Three-dimensional natural convection, mixing and entropy generation in heterogeneous porous medium

Xiangjuan Yang, Qian Shao, Hussein Hoteit, Jesus Carrera, Anis Younes, Marwan Fahs

Three-dimensional natural convection, mixing and entropy generation in heterogeneous porous medium

Xiangjuan Yang[a], Qian Shao[a,*], Hussein Hoteit[b], Jesus Carrera[c], Anis Younes[d], Marwan Fahs[d]

[a] School of Civil Engineering, Wuhan University, 8 South Road of East Lake, Wuchang, 430072 Wuhan, PR China

[b]Physical Science and Engineering Division, King Abdullah University of Science and Technology, Thuwal, Saudi Arabia

[c]Institute of Environmental Assessment and Water Research (IDAEA), CSIC, Barcelona, Spain

[d]LHyGES, Univ. de Strasbourg/EOST/ENGEES, CNRS, 1 rue Blessig, 67084 Strasbourg, France.

*Corresponding author. Email: qian.shao@whu.edu.cn

Submitted to Advances in Water Resources

Abstract

Three-dimensional (3D) natural convection (NC) processes in heterogeneous porous media and associated energy losses and mixing processes are still poorly understood. Studies are limited to two-dimensional domains because of computational burden, worsened by heterogeneity, which may demand grid refinement at high permeability zones for accurate evaluation of buoyancy forces. We develop a meshless Fourier series (FS) solution of the natural convection problem in a porous enclosure driven by thermal or compositional variations. We derive the vector potential formulation of the governing equations for vertical and horizontal heterogeneity of hydraulic conductivity and implement an efficient method to solve the spectral system with an optimized number of Fourier modes. 3D effects are induced either by heterogeneity or variable boundary conditions. The developed FS solution is verified against a finite element solution obtained using COMSOL Multiphysics. We evaluate entropy generation (viscous dissipation and mixing) indicators using Fourier series expansions and assess how they are affected by heterogeneity. We define a large-scale Rayleigh number to account for heterogeneity by adopting an arithmetic average effective permeability. Results show that increasing the Rayleigh number intensifies fluid flow, thus enhancing convective transfer, which causes a dramatic increase in total entropy generation. Both viscous dissipation and mixing (and thus chemical reactions in the solute transport case) increase. The third dimension effect, which also enhances flow and entropy indicators, is more pronounced at high Rayleigh numbers. Surprisingly, entropy variation indicators remain virtually unchanged in response to changes in heterogeneity, for fixed Rayleigh number, which we attribute to the arithmetic average permeability being indeed appropriate for NC in 3D. This study not only explores the effect of Rayleigh number and heterogeneity on natural convection processes and the associated entropy generation and mixing processes, but also provides a highly accurate solution that can be used for codes benchmarking.

Keywords: Natural convection; Entropy generation; Heterogeneous porous media; Three-dimensional; Fourier series method

1 Introduction

Natural convection (NC) takes place in porous media when the saturating fluid density changes due to the variation of temperature and/or composition. Because of its wide applications in environmental, industrial, and engineering fields, NC in porous enclosures caused by thermal effects has been intensively investigated in the past decades. These applications range from the small (micrometers) scale, such as blood flow in the pulmonary alveolar sheet and heating process in solid oxide fuel cells, to the large (meters or kilometers) scale, such as thermal insulation in buildings, CO2 sequestration, aquifers thermal energy storage, seawater intrusion and geothermal or oil reservoirs. Comprehensive surveys on NC in porous media and its industrial and environmental applications can be found in Nield and Simmons [2019], Nield and Bejan [2017], Vafai [2011], Vadász [2008], Ingham and Pop [2005] and Kimura et al. [1997].

Energy losses due to the convective heat transfer, fluid friction, and diffusion effects occur in practical applications involving heat transfer in porous media [Torabi et al., 2017]. This energy loss or the process efficiency can be quantified in terms of entropy generation, based on simultaneous application of the first and second laws of thermodynamics. Entropy generation analysis is usually applied to distinguish between reversible and irreversible processes. By evaluating and minimizing the entropy generation, the overall efficiency of a thermal system can be improved, and losses can be optimized. Special attention has been paid to the study of entropy generation on NC in porous enclosures. The main addressed topics are the influence on entropy generation of enclosure's geometry and boundary conditions [Baytaş, 2000; Kaluri and Basak, 2011; Basak et al., 2012[a,b]; Datta et al., 2016; Chamkha and Selimefendigil, 2018; Chandra Pal, 2018], hydraulic and thermal parameters of the porous medium [Bouabid et al. 2011; Chamkha and Selimefendigil, 2018], different types of fluids under different rheological behaviors [Khan and Gorla, 2011; Al-Zamily, 2017; Mansour et

al., 2017] or internal heat generation [Al-Zamily, 2017]. Mansour et al. [2017] investigated the effect of viscous dissipation. Jbara et al. [2013] studied entropy generation under unsteady conditions. While most studies assume thermal equilibrium between solid and liquid phases of the porous medium, Baytas [2007] addressed entropy generation under non-equilibrium thermal conditions. Entropy generation in MHD nanofluid natural convection has been investigated in Ghasemi and Siavashi [2017]. Oztop and Al-Salem [2012] presented a thorough review of entropy generation in natural and mixed convection. Several studies are concerned with the effect of coupled mass and heat transfer processes (i.e., double-diffusive convection) on entropy generation [Mchirgui et al. 2014; Kefayati, 2016; Hussain et al., 2018].

Two different kinds of processes drive entropy generation on NC problems: dissipation of mechanical energy by viscous forces and loss of variability by diffusion (conduction in thermal convection, or molecular diffusion in solute transport). The latter has received increased attention in the reactive transport literature, where it is termed mixing, because it drives chemical reactions [Rezaei et al., 2005; Cirpka and Valocchi, 2007]. In fact, the rates of fast reactions, driven by the rate at which reacting solutes mix, are proportional to the local entropy generation rate [de Simoni et al., 2005].

Heterogeneity of porous media is known to play a significant role in flow and heat transfer processes. Industrial and natural porous media display spatial variability of thermal and, especially, hydraulic properties, such as permeability and thermal conductivity, which significantly affect water flow and heat transfer. The effect of heterogeneity on NC in porous media has been heavily scrutinized. A widely-discussed topic is the effect of heterogeneity on the onset of NC induced by a vertical density gradient (unstable configuration) [Nield and Simmons, 2007; Nield and Kuznetsov, 2007[a,b],2008, 2011; Nield, 2008; Nield et al. 2009, 2016; Simmons et al., 2010]. The topic is especially relevant for geological CO_2 storage, where density changes when CO_2 is dissolved in native fluids, because dissolution controls

the ultimate fate of CO_2, so that the onset of NC controls whether dissolution is going to be relevant during CO_2 injection [Riaz et al., 2006; Hidalgo et al., 2009, 2012]. Impacts of heterogeneity on the onset of NC under local non-equilibrium conditions have been studied in Nield and Kuznetsov [2015]. Nguyen et al. [2016] studied the effects of heterogeneity on fingering phenomena induced by unstable NC. The influence of heterogeneity on stable configuration of NC (horizontal density gradient) has been the subject of several studies. Marvel and Lai [2010] investigated NC in layered porous cavity. Fahs et al. [2015] studied the effect of stratified heterogeneity on stable natural convection and provided a reference solution for code benchmarking. Fajraoui et al. [2017] performed a global sensitivity analysis to evaluate the effects of uncertainties related to parameters controlling the heterogeneity on convective flow, temperature field, and heat transfer flux.

Most of above-mentioned studies on NC in porous enclosures and related processes' irreversibility are limited to two-dimensional (2D) domains. This 2D assumption is commonly adopted to reduce the computational overheads of three-dimensional (3D) simulations. However, NC processes are three-dimensional by nature. The 2D assumption is only applicable for configurations with specific geometry, boundary conditions, and heterogeneity, where the variations are negligible in the third dimension. With the advancement of computational technology, several 3D numerical studies have been conducted to investigate and understand the three-dimensional NC processes. Pau et al. [2010] demonstrated that the onset time is shorter and the convection rate is larger for 3D simulations than for 2D. Wang et al. [2010] investigated 3D NC in an inclined porous cubic box under time oscillating boundary conditions, where the 3D effect is related to box inclination. They found that the convective flow was quasi-two-dimensional if the box has a moderate inclination angle, while for seriously inclined cases, much more complicated three-dimensional convective flow patterns were observed. Voss et al. [2010] investigated an unstable configuration of NC in an

inclined cubic box and showed the effect of 3D processes on the critical Rayleigh number for the onset of instability. Guerrero-Martínez et al. [2016] studied unstable configuration (vertical density gradient) of an inclined cubic box in both homogeneous and layered porous domains, respectively.

This informal survey indicates evidence of the importance of heterogeneity in controlling NC processes and the significance of entropy generation associated with NC in porous enclosures. It also reveals increasing interest in 3D studies for practical purposes. However, this review also shows that there are still several open research questions related to this topic. Indeed, due to high computational requirements, 3D studies on NC in porous enclosures are scarce. While different properties of domain and boundary conditions could lead to three-dimensional configurations, in the few existing studies, the 3D effects are only induced by box inclination or unstable flow configurations. Furthermore, to deal with computational overheads, existing studies have considered relatively low Rayleigh numbers. In addition, 3D studies on NC processes and associated entropy generation in heterogeneous domains are missing and corresponding processes are still not well-understood. To the best of our knowledge, the only existing work addressing this topic is Zhuang and Zhu [2018]. Nevertheless, that work does not account for real 3D effects as the problem under investigation can be simplified to 2D. The main goal of this work is to address these gaps and to provide a new insight on NC and entropy generation in 3D heterogeneous porous enclosures.

Thus, we study NC and entropy generation in a cubic enclosure filled with a heterogeneous porous medium. This is a problem that has been widely studied in academic research and engineering applications to understand NC processes [Zhao et al., 2005, 2009]. It is also a typical problem that is commonly used as a benchmark to validate numerical codes. We consider two different configurations corresponding to vertical and horizontal heterogeneity, which are common in geological formations [Jiang et al., 2010; Miroshnichenko et al., 2018;

132 Fahs et al., 2015]. Both configurations are effective 3D cases that cannot be simplified to 2D.
133 The 3D effects are induced either by the heterogeneity of the porous domain or boundary
134 conditions. Simulation of three-dimensional NC in porous media is a computationally
135 challenging problem, particularly for high Rayleigh numbers. Heterogeneity compounds these
136 challenges as it leads to locally high permeability zones where the accurate evaluation of
137 buoyancy forces requires unpractical dense computational grids. Accurate evaluation of
138 entropy generation is also a hard computational task because it involves fluxes and space
139 derivatives of the temperature, which requires appropriate numerical techniques [Younes et al.,
140 2010]. Thus, to avoid computational limitations and numerical artifacts of conventional
141 methods, we develop an efficient and accurate meshless solution based on the Fourier series
142 method (FS) applied to the vector potential formulation of the governing equation [Peyret,
143 2002; Shao et al., 2018]. We extend the vector potential formulation developed by Shao et al.
144 [2018] to the heterogeneous domain and we use an efficient technique to reduce the number
145 of Fourier series modes. Contrarily to the homogeneous domain, heterogeneity leads to full
146 non-zero vector potential. We use appropriate techniques to efficiently solve the spectral
147 system. This includes a simplified evaluation of the nonlinear convective terms, the use of an
148 efficient nonlinear solver, and parallel implementation of the FS method. Entropy generation
149 is evaluated analytically based on the Fourier series expansion. The developed FS solution is
150 verified by comparison against COMSOL Multiphysics. Taking advantage of the accuracy of
151 the FS solution, we provide high-quality data that can be used as a reference for the validation
152 of numerical codes dealing with NC and entropy generation. This represents an important
153 feature of this work, as reference benchmark solutions for entropy generation are lacking. Due
154 to its high performance, the FS solution is used to i) develop a parametric study, ii) to
155 understand the effect of heterogeneity on metrics characterizing temperature, heat flux,

156 convective flow, mixing, and entropy generation, and iii) to evaluate the significance of the
157 3D processes by comparing 3D and 2D simulations.

158 ## 2 Problems description and governing equations

159 We consider a cubic saturated porous enclosure of size H, as shown in Fig. 1, where fluid
160 flows in response to density variations caused by variations in temperature or concentration.
161 For simplicity, we adopt heat transfer nomenclature, but the problem is mathematically
162 equivalent to solute mass transfer. All domain boundaries are assumed impermeable, that is,
163 convective fluxes across the six sides are zero. Two different configurations of heterogeneity
164 are investigated in this work (Fig. 1). In the first configuration (V-het), the enclosure is filled
165 with vertically stratified porous media, so that its permeability varies along the y coordinate
166 (i.e., $k_p = k_p(y)$). The enclosure is subject to constant but distinct temperatures on two opposite
167 boundaries, i.e., $T=T_h$ at $x=0$ and $T=T_c$ at $x=H$, as shown in Fig. 1(a). In the second
168 configuration (H-het), the enclosure is filled with horizontally stratified porous media, so that
169 its permeability is a function of z. This configuration can be simplified to 2D. But, as our
170 objective is to investigate effective 3D cases, we assume varying boundary temperature on
171 one side (i.e., $T=F(y)$ at $x=0$), and constant temperature on the opposite side (i.e., $T=T_c$ at
172 $x=H$), as shown in Fig. 1(b). Variable temperature boundary conditions are common in the
173 simulations of geothermal reservoirs. The two configurations allow us to investigate the 3D
174 effects induced either by heterogeneity or from the varying temperature boundary conditions.

175

176

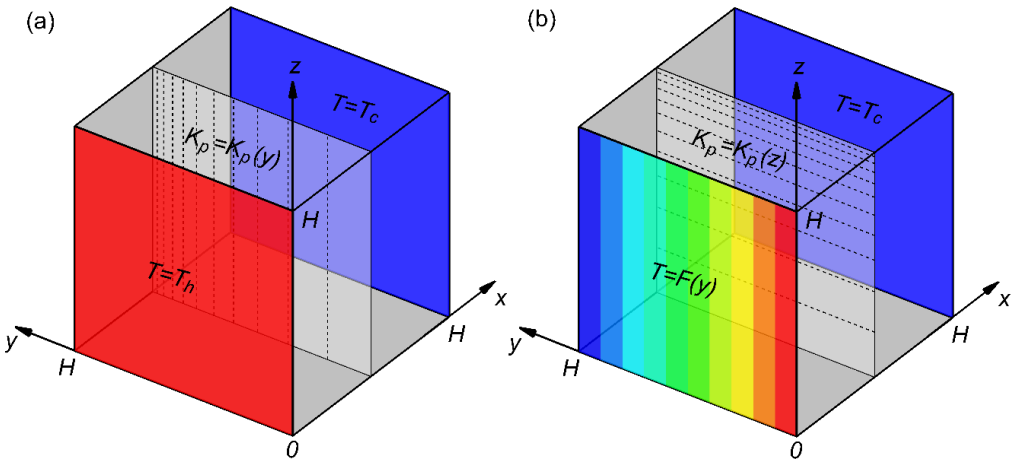

Fig. 1. Schematic description of the two cubic porous enclosures and their boundary conditions: (a) an enclosure filled by vertically stratified porous media with constant but distinct temperatures on the opposite boundaries (V-het); (b) an enclosure filled by horizontally stratified porous media with varying temperature on one side, and constant temperature on the opposite side (H-het).

The mathematical model describing the NC processes in saturated porous media is based on the mass conservation equation, Darcy's law, and the heat transfer equation. Adopting the Boussinesq approximation and steady-state fluid flow, these equations can be written as:

$$\nabla \cdot \mathbf{q} = 0 \tag{0}$$

$$\mathbf{q} = -\frac{k_p}{\mu}\left(\nabla p - \rho_c g \beta \left(T - T_c\right)\mathbf{e_z}\right) \tag{0}$$

$$C_m \frac{\partial T}{\partial t} + C_f \mathbf{q} \cdot \nabla T = \lambda_m \nabla \cdot \nabla T \tag{0}$$

where $\mathbf{q}$ $\left[\mathrm{LT}^{-1}\right]$ is water flux (Darcy velocity), μ $\left[\mathrm{ML}^{-1}\mathrm{T}^{-1}\right]$ is the dynamic viscosity of the fluid, p $\left[\mathrm{ML}^{-1}\mathrm{T}^{-2}\right]$ is pressure, ρ_c $\left[\mathrm{ML}^{-3}\right]$ is the density of fluid at the reference temperature T_c, g $\left[\mathrm{LT}^{-2}\right]$ is the gravity acceleration, β $\left[\Theta^{-1}\right]$ is the thermal expansion coefficient, k_p $\left[\mathrm{L}^2\right]$ is the permeability, which depends on the properties of the porous media and may vary in space, t $\left[\mathrm{T}\right]$ is time, C_f $\left[\mathrm{L}^{-1}\mathrm{MT}^{-2}\Theta^{-1}\right]$ is the thermal capacity (specific heat times density) of the fluid, C_m $\left[\mathrm{L}^{-1}\mathrm{MT}^{-2}\Theta^{-1}\right]$ and λ_m $\left[\mathrm{MLT}^{-3}\Theta^{-1}\right]$ are the thermal capacity

(specific heat times density) and the effective thermal conductivity of the porous medium, respectively. The latter is obtained by averaging the thermal capacity and conductivity of the fluid and solid phases, weighted by the porosity ε:

$$C_{\mathrm{m}}=\varepsilon C_{\mathrm{f}}+\left(1-\varepsilon\right)C_{\mathrm{s}} \tag{0}$$

$$\lambda_{\mathrm{m}}=\varepsilon\lambda_{\mathrm{f}}+\left(1-\varepsilon\right)\lambda_{\mathrm{s}} \tag{0}$$

Subscripts m, s, and f represent the porous medium, solid, and fluid, respectively. The density of the fluid is a linear function of temperature:

$$\rho=\rho_{\mathrm{c}}\left(1-\beta\left(T-T_{\mathrm{c}}\right)\right) \tag{0}$$

The boundary conditions of the two aforementioned configurations (V-het and H-het) are defined in Table 1, where q_x, q_y, and q_z are the water flux components in the *x*-, *y*-, and *z*-directions, respectively.

Table 1. Boundary conditions of the two configurations showing the variable prescribed temperature at the *x*=0 face.

Configuration	$x=0$	$x=H$	$y=0,H$	$z=0,H$
V-het	$q_x=0,\ T=T_h$	$q_x=0,\ T=T_{\mathrm{c}}$	$q_y=0,\ \dfrac{\partial T}{\partial y}=0$	$q_z=0,\ \dfrac{\partial T}{\partial z}=0$
H-het	$q_x=0,\ T=F\left(y\right)$			

3 Fourier series solution

The Fourier series method is used to solve the governing equations for both configurations V-het (vertical heterogeneity) and H-het (horizontal heterogeneity). The solution procedure is as follows. First, governing equations are expressed in terms the vector potential. Second, a change of variables is made to ensure periodic-homogeneous boundary conditions for both flow and heat transfer. Third, the temperature and the components of the vector potential are expanded using Fourier series truncated at given orders, which are then substituted into the governing equations. After the Galerkin treatment, a system of nonlinear equations with the

Fourier series coefficients as unknowns is generated. Eventually, solving the system of equations, one obtains the vector potential and the temperature field expressed analytically in terms of Fourier coefficients.

3.1 The vector potential formulation

At steady state, Darcy's velocity $\mathbf{q}$ admits a vector potential $\boldsymbol{\varphi}$ such that $\mathbf{q}=\nabla\times\boldsymbol{\varphi}$. According to the continuity equation, the vector potential satisfies $\nabla\cdot\mathbf{q}=\nabla\cdot\left(\nabla\times\boldsymbol{\varphi}\right)=0$. Applying the *curl* operator on Darcy's law, one can eliminate the fluid pressure in the flow equation as $\nabla\times\nabla p=0$. Further, considering a solenoidal vector potential as shown in Guerrero-Martínez et al. [2016] and Shao et al. [2018] leads to $\nabla\cdot\boldsymbol{\varphi}=0$. Then assuming the permeability satisfies the function $K_p=K_p\left(y,z\right)$ due to the heterogeneity of the porous medium, one obtains the steady-state flow equations in terms of vector potential components:

$$\begin{cases}\nabla^2\varphi_x+\dfrac{1}{k_p}\left(\dfrac{\partial k_p}{\partial y}\left(\dfrac{\partial\varphi_y}{\partial x}-\dfrac{\partial\varphi_x}{\partial y}\right)-\dfrac{\partial k_p}{\partial z}\left(\dfrac{\partial\varphi_x}{\partial z}-\dfrac{\partial\varphi_z}{\partial x}\right)\right)+\dfrac{\rho_c g k_p\beta}{\mu}\dfrac{\partial T}{\partial y}=0\\ \nabla^2\varphi_y+\dfrac{1}{k_p}\dfrac{\partial k_p}{\partial z}\left(\dfrac{\partial\varphi_z}{\partial y}-\dfrac{\partial\varphi_y}{\partial z}\right)-\dfrac{\rho_c g k_p\beta}{\mu}\dfrac{\partial T}{\partial x}=0\\ \nabla^2\varphi_z-\dfrac{1}{k_p}\dfrac{\partial k_p}{\partial y}\left(\dfrac{\partial\varphi_z}{\partial y}-\dfrac{\partial\varphi_y}{\partial z}\right)=0\end{cases} \tag{0}$$

Substituting the vector potential into Eq. (3), we simplify the steady-state heat transfer equation to:

$$\left(\nabla\times\boldsymbol{\varphi}\right)\cdot\nabla T=\alpha\nabla\cdot\nabla T \tag{0}$$

where $\alpha=\lambda_{\mathrm{m}}/C_{\mathrm{f}}$ represents the effective thermal diffusivity. Then we define the following dimensionless variables:

$$\boldsymbol{\psi}=\frac{\boldsymbol{\varphi}}{\alpha},\ \vartheta=\frac{T-T_{\mathrm{c}}}{\Delta T},\ X=\frac{x}{H},\ Y=\frac{y}{H},\ Z=\frac{z}{H} \tag{0}$$

where $\Delta T = T_{\mathrm{h}} - T_{\mathrm{c}}$ is the temperature difference between the hot and cold walls. Using the above non-dimensional variables, we obtain the dimensionless steady-state flow and heat transfer equations as follows:

$$\begin{cases} \nabla^2 \psi_X + \dfrac{1}{k_p}\left(\dfrac{\partial k_p}{\partial Y}\left(\dfrac{\partial \psi_Y}{\partial X} - \dfrac{\partial \psi_X}{\partial Y}\right) - \dfrac{\partial k_p}{\partial Z}\left(\dfrac{\partial \psi_X}{\partial Z} - \dfrac{\partial \psi_Z}{\partial X}\right)\right) + Ra\dfrac{\partial \vartheta}{\partial Y} = 0 \\ \nabla^2 \psi_Y + \dfrac{1}{k_p}\dfrac{\partial k_p}{\partial Z}\left(\dfrac{\partial \psi_Z}{\partial Y} - \dfrac{\partial \psi_Y}{\partial Z}\right) - Ra\dfrac{\partial \vartheta}{\partial X} = 0 \\ \nabla^2 \psi_Z - \dfrac{1}{k_p}\dfrac{\partial k_p}{\partial Y}\left(\dfrac{\partial \psi_Z}{\partial Y} - \dfrac{\partial \psi_Y}{\partial Z}\right) = 0 \end{cases} \tag{0}$$

$$\left(\nabla \times \boldsymbol{\psi}\right) \cdot \nabla \vartheta = \nabla \cdot \nabla \vartheta \tag{0}$$

where $Ra = \rho_{\mathrm{c}} g k_p H \beta \Delta T / (\mu \alpha)$ is the local thermal Rayleigh number that is dependent on the variation of permeability in heterogeneous porous media.

These equations are similar to those of Shao et al. [2018], except for the terms involving the *z*-component of the vector potential that can be dropped out in homogeneous domains. Here we show that, due to heterogeneity, all the components of the vector potential should be considered.

3.2 Homogeneous boundary conditions

The flow boundary conditions are derived in terms of vector potential. As it is shown in Guerrero-Martínez et al. [2016] and Shao et al. [2018], the flow boundary conditions can be written as follows:

$$\begin{aligned} &\frac{\partial \psi_X}{\partial X} = \psi_Y = \psi_Z = 0, \quad \text{at } X = 0,1 \\ &\frac{\partial \psi_Y}{\partial Y} = \psi_X = \psi_Z = 0, \quad \text{at } Y = 0,1 \\ &\frac{\partial \psi_Z}{\partial Z} = \psi_X = \psi_Z = 0, \quad \text{at } Z = 0,1 \end{aligned} \tag{0}$$

Note that these homogeneous impervious boundary conditions for fluid flow are applicable for both configurations V-het and H-het. To derive homogeneous boundary conditions for heat transfer, we express the temperature boundary conditions in terms of dimensionless variables:

$$\begin{cases} \vartheta = f(Y), \text{ at } X = 0 \\ \vartheta = 0, \quad \text{at } X = 1 \end{cases} \quad \frac{\partial \vartheta}{\partial Y} = 0, \text{ at } Y = 0,1 \quad \frac{\partial \vartheta}{\partial Z} = 0, \text{ at } Z = 0,1 \tag{0}$$

where $f(Y)$ is a constant $f(Y) = 1$ for the V-het configuration, and defined as $f(Y) = \left(F(y) - T_c\right) / \left(T_h - T_c\right)$ for the H-het configuration. Further, we define the following change of variable:

$$\theta = \vartheta + (X - 1) f(Y) \tag{0}$$

Using the above equation, the boundary conditions in terms of the shifted dimensionless temperature θ become:

$$\begin{aligned} &\theta = 0, && \text{at } X = 0,1 \\ &\frac{\partial \theta}{\partial Y} = (X - 1) f'(Y), && \text{at } Y = 0,1 \\ &\frac{\partial \theta}{\partial Z} = 0, && \text{at } Z = 0,1 \end{aligned} \tag{0}$$

These temperature boundary conditions are periodic when the function $f(Y)$ satisfies the condition $f'(0) = f'(1) = 0$. For the V-het configuration, as $f(Y) = 1$, this condition is satisfied in nature. For the H-het configuration, to meet this requirement, we select a particular function such that:

$$f(Y) = \frac{1 + \cos(\pi Y)}{2} \tag{0}$$

Note that the presented method is not limited to this particular function. Any other function that leads to periodic boundary conditions is applicable. Substituting Eq. (14) into Eqs. (10)

and (11), one obtains the final system of governing equations in terms of the shifted temperature θ and vector potential components:

$$\nabla^2\psi_X+\frac{1}{k_p}\left(\frac{\partial k_p}{\partial Y}\left(\frac{\partial \psi_Y}{\partial X}-\frac{\partial \psi_X}{\partial Y}\right)-\frac{\partial k_p}{\partial Z}\left(\frac{\partial \psi_X}{\partial Z}-\frac{\partial \psi_Z}{\partial X}\right)\right)+Ra\frac{\partial \theta}{\partial Y}-Ra\left(X-1\right)f'\left(Y\right)=0 \tag{0}$$

$$\nabla^2\psi_Y+\frac{1}{k_p}\frac{\partial k_p}{\partial Z}\left(\frac{\partial \psi_Z}{\partial Y}-\frac{\partial \psi_Y}{\partial Z}\right)-Ra\frac{\partial \theta}{\partial X}+Ra\cdot f\left(Y\right)=0 \tag{0}$$

$$\nabla^2\psi_Z-\frac{1}{k_p}\frac{\partial k_p}{\partial Y}\left(\frac{\partial \psi_Z}{\partial Y}-\frac{\partial \psi_Y}{\partial Z}\right)=0 \tag{0}$$

$$\begin{aligned}&\left(\frac{\partial \psi_Z}{\partial Y}-\frac{\partial \psi_Y}{\partial Z}\right)\frac{\partial \theta}{\partial X}+\left(\frac{\partial \psi_X}{\partial Z}-\frac{\partial \psi_Z}{\partial X}\right)\frac{\partial \theta}{\partial Y}+\left(\frac{\partial \psi_Y}{\partial X}-\frac{\partial \psi_X}{\partial Y}\right)\frac{\partial \theta}{\partial Z}-\left(\frac{\partial^2\theta}{\partial X^2}+\frac{\partial^2\theta}{\partial Y^2}+\frac{\partial^2\theta}{\partial Z^2}\right)\\&-\left(\frac{\partial \psi_Z}{\partial Y}-\frac{\partial \psi_Y}{\partial Z}\right)f\left(Y\right)-\frac{\partial \psi_X}{\partial Z}\left(X-1\right)f'\left(Y\right)+\left(X-1\right)f''\left(Y\right)=0\end{aligned} \tag{0}$$

3.3 The spectral system

The components of the vector potential ψ_X, ψ_Y, and ψ_Z, as well as the shifted temperature θ are expanded using infinite triple Fourier series that are truncated at given orders:

$$\psi_X\left(X,Y,Z\right)=\sum_{i=0}^{Ni}\sum_{j=1}^{Nj}\sum_{k=1}^{Nk}A_{i,j,k}\cos\left(i\pi X\right)\sin\left(j\pi Y\right)\sin\left(k\pi Z\right) \tag{0}$$

$$\psi_Y\left(X,Y,Z\right)=\sum_{l=1}^{Nl}\sum_{m=0}^{Nm}\sum_{n=1}^{Nn}B_{l,m,n}\sin\left(l\pi X\right)\cos\left(m\pi Y\right)\sin\left(n\pi Z\right) \tag{0}$$

$$\psi_Z\left(X,Y,Z\right)=\sum_{d=1}^{Nd}\sum_{r=1}^{Nr}\sum_{s=0}^{Ns}C_{d,r,s}\sin\left(d\pi X\right)\sin\left(r\pi Y\right)\cos\left(s\pi Z\right) \tag{0}$$

$$\theta\left(X,Y,Z\right)=\sum_{u=1}^{Nu}\sum_{v=0}^{Nv}\sum_{w=0}^{Nw}E_{u,v,w}\sin\left(u\pi X\right)\cos\left(v\pi Y\right)\cos\left(w\pi Z\right) \tag{0}$$

where Ni, Nj and Nk are the truncation orders for the vector potential component ψ_X in the X-, Y- and Z-directions. Similarly, Nl, Nm and Nn (resp. Nd, Nr and Ns) are that for ψ_Y (resp. ψ_Z). Nu, Nv and Nw are the truncation orders for the dimensionless temperature

θ. $A_{i,j,k}$, $B_{l,m,n}$, $C_{d,r,s}$ and $E_{u,v,w}$ are the Fourier series coefficients for the vector potential components ψ_X, ψ_Y, ψ_Z, and the temperature θ, respectively. It should be noted that all the above Fourier series expansions honor the periodic flow and temperature boundary conditions as shown in Eqs. (12) and (15).

The Fourier series expansions are substituted into Eqs. (17)-(20), and followed by the Galerkin treatment, where the resulted equations are multiplied, respectively, by the following trial functions that use Fourier modes:

$$
\begin{aligned}
&\Lambda^{\psi_X}_{I,J,K} = 8\cos(I\pi X)\sin(J\pi Y)\sin(K\pi Z) \qquad I=0,...,Ni,\ J=1,...,Nj,\ K=1,...,Nk\\
&\Lambda^{\psi_Y}_{L,M,N} = 8\sin(L\pi X)\cos(M\pi Y)\sin(N\pi Z) \quad L=1,...,Nl,\ M=0,...,Nm,\ N=1,...,Nn\\
&\Lambda^{\psi_Z}_{D,R,S} = 8\sin(D\pi X)\sin(R\pi Y)\cos(S\pi Z) \qquad D=1,...,Nd,\ R=1,...,Nr,\ S=0,...,Ns\\
&\Lambda^{\theta}_{U,V,W} = 8\sin(U\pi X)\cos(V\pi Y)\cos(W\pi Z) \quad U=1,...,Nu,\ V=0,...,Nv,\ W=0,...,Nw
\end{aligned}
\tag{0}
$$

The resulted equations are then integrated over the cubic domain. To allow an analytical evaluation of all the triple integrations arising from the FS method, we assume that permeability depends on space by means of an exponential function [Jiang et al., 2010; Fahs et al., 2015; Zhuang and Zhu, 2018]:

$$k_p(Y,Z) = k_0 e^{\sigma Y + \varsigma Z} \tag{0}$$

where k_0 is the permeability at $Y=Z=0$, and σ and ς are the changing rate of $\ln(K_p)$ in the Y and Z direction, respectively. When $\sigma=\varsigma=0$, permeability is homogeneous over the domain. With $\sigma\neq 0$ and $\varsigma=0$, the porous medium is vertically stratified, and permeability varies in the Y direction, which is the case in the V-het configuration as shown in Fig. 1(a). While with $\sigma=0$ and $\varsigma\neq 0$, the porous medium is horizontally stratified, which is the case in the H-het configuration as shown in Fig. 1(b).

Eq. (25) allows us to integrate all Fourier integrals analytically, resulting in a system of nonlinear algebraic equations with the Fourier coefficients $A_{i,j,k}$, $B_{l,m,n}$, $C_{d,r,s}$, and $E_{u,v,w}$ as

unknowns. For the V-het configuration, the corresponding boundary condition and the permeability are set as $f(Y)=1$ and $k_p = k_0 e^{\sigma Y}$, leading to the following residual equations:

$$\begin{aligned} RFX_{I,J,K} = & -\pi^2\left(I^2+\alpha_I J^2+\alpha_I K^2\right)A_{I,J,K} \\ & -\sigma\left(\alpha_I\sum_{j=1}^{Nj} j.A_{I,j,K}\Phi_{J,j} - I.\sum_{m=0}^{Nm} B'_{I,m,K}\Phi_{J,m}\right) \\ & -\frac{Ra_0}{\pi}\sum_{u=1}^{Nu}\sum_{v=0}^{Nv}\sum_{w=0}^{Nw} v.E_{u,v,w}\Phi_{u,I}\Pi_{v,J}\Phi_{K,w}=0 \\ & \left(I=0,...,Ni,\ J=1,...,Nj,\ K=1,...,Nk\right) \end{aligned} \tag{0}$$

$$\begin{aligned} RFY_{L,M,N} = & -\pi^2\left(\alpha_M L^2+M^2+\alpha_M N^2\right)B_{L,M,N} \\ & -\frac{Ra_0}{\pi}\sum_{u=1}^{Nu}\sum_{v=0}^{Nv}\sum_{w=0}^{Nw} u.E_{u,v,w}\Phi_{L,u}\Upsilon_{v,M}\Phi_{N,w} \\ & +\frac{Ra_0}{\pi^2}\Phi_{L,0}\Upsilon_{M,0}\Phi_{N,0}=0 \\ & \left(L=1,...,Nl,M=0,...,Nm,N=1,...,Nn\right) \end{aligned} \tag{0}$$

$$\begin{aligned} RFZ_{D,R,S} = & -\pi^2 C_{D,R,S}\left(\alpha_S D^2+\alpha_S R^2+S^2\right) \\ & +\sigma\left(S.\sum_{m=0}^{Nm} B'_{D,m,S}\Phi_{R,m} - \alpha_S.\sum_{r=0}^{Nr} rC_{D,r,S}\Phi_{R,r}\right)=0 \\ & \left(D=1,...,Nd,\ R=1,...,Nr,\ S=0,...,Ns\right) \end{aligned} \tag{0}$$

$$\begin{aligned} RT_{U,V,W} = & \pi\left(\alpha_V.W.B'_{U,V,W} - \alpha_W.V.C'_{U,V,W}\right) - \pi^2\left(\alpha_W\alpha_V U^2+\alpha_W V^2+\alpha_V W^2\right)E_{U,V,W} \\ & +\frac{\pi^2}{8}\sum_{u=1}^{Nu}\sum_{v=0}^{Nv}\sum_{w=0}^{Nw} E_{u,v,w}\left[\sum_{i=0}^{Ni}\sum_{j=1}^{Nj}\sum_{k=1}^{Nk} A_{i,j,k}\left(k.v.\xi_{i,u,U}.\kappa_{j,v,V}.\upsilon_{k,w,W} - j.w.\xi_{i,u,U}.\upsilon_{j,v,V}.\kappa_{k,W,w}\right)\right. \\ & -\sum_{l=1}^{Nl}\sum_{m=0}^{Nm}\sum_{n=1}^{Nn} B_{l,m,n}\left(n.u.\kappa_{l,U,u}.\zeta_{m,v,V}.\upsilon_{n,w,W} - l.w.\xi_{l,u,U}.\zeta_{m,v,V}.\kappa_{n,w,W}\right) \\ & \left.+\sum_{d=1}^{Nd}\sum_{r=1}^{Nr}\sum_{s=0}^{Ns} C_{d,r,s}\left(r.u.\kappa_{d,U,u}.\upsilon_{r,v,V}.\upsilon_{s,w,W} - d.v.\xi_{d,u,U}.\kappa_{r,v,V}.\zeta_{s,w,W}\right)\right]=0 \\ & \left(U=1,...,Nu,V=0,...,Nv,W=0,...,Nw\right) \end{aligned} \tag{0}$$

where *RFX*, *RFY*, *RFZ*, and *RT* are the residuals corresponding to the three flow components and heat transfer equations, respectively. Ra_0 in Eqs. (26) and (27) is the thermal Rayleigh number at Y=0 and Z=0, defined as:

$$Ra_0 = \frac{\rho_c g k_0 H \beta \Delta T}{\mu \alpha} \tag{30}$$

For the V-het configuration, Ra_0 represents the Rayleigh number based on the permeability of the lower layer (Z=0), while for the H-het configuration it is the Rayleigh number based on the permeability of the vertical wall Y=0.

The residuals for the H-het configuration and the corresponding coefficients in these equations are given in the Section S1 of Supplemental Material. We solve the system of nonlinear equations using a nonlinear solver from the IMSL library based on the modified Powell hybrid algorithm (https://docs.roguewave.com/imsl/fortran/7.1/html/fnlmath/index.html), which is very efficient. We include analytical evaluation of the Jacobian matrix to improve the performance and convergence of the solver (see Supplemental Material Section S2). Besides, Eq. (29) involves terms that have six overlapped summations, which are computationally expensive. We simplify these terms from six to three nested summations, as in Shao et al. [2018], to reduce computations. Indeed, this reformulation reduces CPU-time by 2 to 3 orders of magnitude. Finally, parallel computing is implemented in these FG solutions to further reduce the CPU time.

3.4 Metrics for the assessment of convective flow, heat transfer and entropy generation

The convective flow is assessed using the dimensionless velocity defined as follows:

$$\mathbf{Q} = \frac{H}{\alpha}\mathbf{q} \tag{31}$$

The heat transfer performance is evaluated by the average Nusselt number that assesses the heat diffusion across the boundary X=0 into the domain. The local Nusselt number is defined by

$$Nu = \frac{1}{\vartheta_{surf}} \frac{\partial \vartheta}{\partial X}\bigg|_{X=0} \tag{32}$$

where ϑ_{surf} is the imposed average temperature at the boundary X=0. For the V-het configuration, the average temperature at X=0 is $\vartheta_{surf}=1$. While for the H-het configuration, we have $\vartheta_{surf}=\int_0^1\int_0^1 f(Y)\mathrm{d}X\mathrm{d}Z=1/2$. Using the Fourier series expansion of temperature, we obtain the local Nusselt number expressed by Fourier coefficients:

$$Nu=\frac{\pi}{\vartheta_{surf}}\sum_{u=1}^{Nu}\sum_{v=0}^{Nv}\sum_{w=0}^{Nw}uE_{u,v,w}\cos(v\pi Y)\cos(w\pi Z)-\frac{f(Y)}{\vartheta_{surf}} \tag{33}$$

And the average Nusselt number is computed as follows:

$$\overline{Nu}=\int_0^1\int_0^1 Nu.dYdZ=\frac{\pi}{\vartheta_{surf}}\sum_{u=1}^{Nu}uE_{u,0,0}-1 \tag{34}$$

In the considered NC system, the associated entropy generation is due to heat transfer and Darcy dissipation. It can be computed by the evaluation of the time derivative of the temperature or concentration variance [Le borgne et al., 2010] under very specific transient conditions, but not for the steady-state case considered herein. Based on the local thermodynamic equilibrium of the linear transport theory, the local entropy generation for the 3D natural convection is given by Baytaş [2000] and Ghachem et al. [2012]:

$$S_E=\frac{\lambda_{\mathrm{m}}}{T_{\mathrm{c}}^2}\left[\left(\frac{\partial T}{\partial x}\right)^2+\left(\frac{\partial T}{\partial y}\right)^2+\left(\frac{\partial T}{\partial z}\right)^2\right]+\frac{\mu}{T_{\mathrm{c}}k_p}\left(q_x^2+q_y^2+q_z^2\right) \tag{35}$$

Note that the first term evaluates the tendency to temperature homogeneity, which is proportional to the time derivative of temperature variance in transient problems [Le borgne et al., 2010], while the second terms equal the viscous dissipation of energy, divided by T_{c}. The first term is especially relevant in solute mass transfer, where it is termed mixing rate, because mixing controls fast reactions, whose rate is limited by the rate at which reactants mix [De Simoni et al., 2005]. Using the change of variable, we obtain the local entropy generation in terms of dimensionless variables. And then we define the local entropy generation number as:

$$N_E = \underbrace{\left(\frac{\partial\theta}{\partial X} - f(Y)\right)^2 + \left(\frac{\partial\theta}{\partial Y} - (X-1)f'(Y)\right)^2 + \left(\frac{\partial\theta}{\partial Z}\right)^2}_{N_T} + \underbrace{\phi\left(Q_X^2 + Q_Y^2 + Q_Z^2\right)}_{N_F} \tag{36}$$

where Q_X, Q_Y, and Q_Z are dimensionless velocity components in the *X*, *Y*, and *Z* directions, respectively. And ϕ is the local irreversibility distribution ratio that depends on the variation of permeability in heterogeneous porous media:

$$\phi = \frac{\mu T_c \alpha^2}{\lambda_m (\Delta T)^2 k_p} \tag{37}$$

At *Y*=0 and *Z*=0, we have $\phi_0 = \left(\mu T_c \alpha^2\right) \Big/ \left(\lambda_m (\Delta T)^2 k_0\right)$. It is noted that the value of ϕ_0 is dependent on the thermal Rayleigh number (Ra_0). In this work, as in Baytaş [2000], we take:

$$\phi_0 = \frac{10}{Ra_0} \tag{38}$$

In Eq. (36), N_T and N_F represent the irreversibility caused by mixing (dimensionless mixing rate) and Darcy dissipation (dimensionless viscous dissipation), respectively. Based on these, the Bejan number $Be = N_T / N_E$ that denotes the ratio of heat transfer irreversibility to the local entropy generation is defined. If the Bejan number is over 0.5, it implies that the irreversibility due to heat transfer plays a more important role in the entropy generation; otherwise, the irreversibility caused by fluid flow makes the dominant contribution. Furthermore, to assess the overall entropy generation in the domain, the total entropy generation number and the average Bejan number in the cubic enclosure are computed by:

$$N_{tot} = \int_0^1 \int_0^1 \int_0^1 N_E \mathrm{d}X\mathrm{d}Y\mathrm{d}Z \tag{39}$$

$$\overline{Be} = \int_0^1 \int_0^1 \int_0^1 Be \mathrm{d}X\mathrm{d}Y\mathrm{d}Z \tag{40}$$

4 Results and discussion

Three targets are discussed in this section. As a new code has been developed for the FS solution, we first verify the correctness of this code by comparison against finite element (FE) solutions obtained using COMSOL Multiphysics. Secondly, we present high-quality data that can be used as reference solutions for benchmarking numerical models dealing with NC, mixing, and entropy generation in heterogeneous porous domains. Then, taking advantage of the developed FS solution, we investigate the influence of heterogeneity and Rayleigh number on NC and processes irreversibility, and we evaluate the significance of the 3D processes by comparing 2D and 3D simulations.

As can be deduced from the dimensionless governing equations, NC processes and associated entropy generation are controlled by three parameters: the local Rayleigh number Ra_0, the heterogeneity structure (parameterized here in terms of σ for the V-het configuration and ς for the H-het configuration) and the local irreversibility distribution ratio (ϕ_0). The latter is linked to Ra_0 as in Eq. (38). For an adequate analysis, in our investigation, we replace Ra_0 by the effective large-scale Rayleigh number defined based on the average permeability as follows:

$$\overline{Ra} = \frac{\rho_c g \overline{k_p} H \beta \Delta T}{\mu \alpha} \tag{41}$$

where $\overline{k_p} = \int_0^1 \int_0^1 \int_0^1 k_p(Y,Z)\mathrm{d}X\mathrm{d}Y\mathrm{d}Z$ is the large-scale average permeability in the cubic enclosure. The choice is non-trivial, and the effective value of permeability (i.e., the value of homogeneous permeability allowing the same flux through the medium as the actual permeability) has been the subject of research in the oil and hydrology literature [Noetinger, 1994; Renard and de Marsily, 1997; Sanchez-Vila et al., 2006]. What has been found is that the appropriate averaging of permeability depends on the flow dimension. In 1D, the effective permeability is the harmonic average (k_H). In 2D, the effective permeability is the geometric

403 average (k_G). In 3D, the effective permeability is the 1/3 power average ($k_{1/3}$). The arithmetic
404 average adopted here (k_A) is only appropriate for mathematically ideal infinite dimensions.
405 When heterogeneity is large, these averages can be very different. Herein we analyze cases
406 with $\sigma = 2$, where the largest permeability is 7.4 larger than the smallest one and the above
407 four averages (k_A, $k_{1/3}$, k_G, and k_H) equal 3.2, 2.9, 2.7, and 2.3, respectively, which are not
408 significantly different. Then we analyze cases with $\sigma = 4$, where the largest permeability is
409 54.6 larger than the smallest one, and the above averages now equal 13.4, 9.2, 7.4, and 4.1,
410 which are not dramatically different either. For a given heterogeneity, the large-scale
411 Rayleigh number is proportional to the adopted effective permeability. As we shall see, when
412 the large-scale Rayleigh number ($\overline{Ra}$) is constant, entropy indicators remain virtually
413 unchanged when the heterogeneity rate is changed. However, they would increase
414 dramatically if we had adopted any other average for effective permeability, because k_0 would
415 have to be increased in order to maintain the large-scale Rayleigh number unchanged,
416 Thus in all our simulations, we consider the large-scale Rayleigh number ($\overline{Ra}$) and the rate of
417 heterogeneity (σ or ς) as primary parameters controlling physical processes. Based on these
418 parameters, we evaluate the parameters such as the local Rayleigh number (Ra_0) and the local
419 irreversibility distribution ratio (ϕ_0).

420 *4.1 Verification of the FS solution*

421 The number of Fourier modes may affect the accuracy of the FS solutions. We adopt the
422 technique developed by Fahs et al. [2015] to determine the appropriate Fourier modes leading
423 to stable solutions. This technique proceeds by increasing the number of Fourier modes until
424 reaching stable solutions. For the sake of simplicity, we adopt the same number of Fourier
425 coefficients for ψ_X , ψ_Y , ψ_Z , and θ, that is $NX=Ni+1=Nl=Nd=Nu$, $NY=Nj=Nm+1=Nr=Nv+1$,
426 and $NZ=Nk=Nn=Ns+1=Nw+1$. Accordingly, several levels of truncations orders with

427 increasing values of *NX*, *NY*, and *NZ* are tested and the stability is assessed based on the
428 sensitivity of the average Nusselt number ($\overline{Nu}$) to the Fourier modes. Fig. 2 exemplifies the
429 convergence behavior of the FS solution. It shows the variation of $\overline{Nu}$ versus the total number
430 of Fourier modes for three test cases of the V-het configuration, with $\overline{Ra}=100$ and three
431 levels of heterogeneity. It is found that for $\sigma=0$, 2, and 4, the converged FS solutions with
432 stable $\overline{Nu}$ values are obtained with 6,084 (*NX*=24, *NY*=3, and *NZ*=21), 8,640 (*NX*=30, *NY*=3,
433 and *NZ*=24), and 11,232 (*NX*=39, *NY*=3, and *NZ*=24) Fourier modes, respectively. Typically,
434 the increase of the rate of heterogeneity leads to a higher local Rayleigh number, and thus
435 enhances the thermal convection at high permeable zones. For instance, with $\overline{Ra}=100$ and
436 $\sigma=4$, the maximum local Rayleigh number in the domain can reach more than 400. In
437 convection-dominant problems, a large number of Fourier modes is usually required to avoid
438 Gibbs phenomenon and to obtain oscillation-free results [Peyret, 2002]. We should mention
439 that the most important truncation order controlling oscillations is *NX*. Similar behaviours of
440 the FS solution have been observed for the H-het configuration but they are not presented here
441 for the sake of brevity.
442

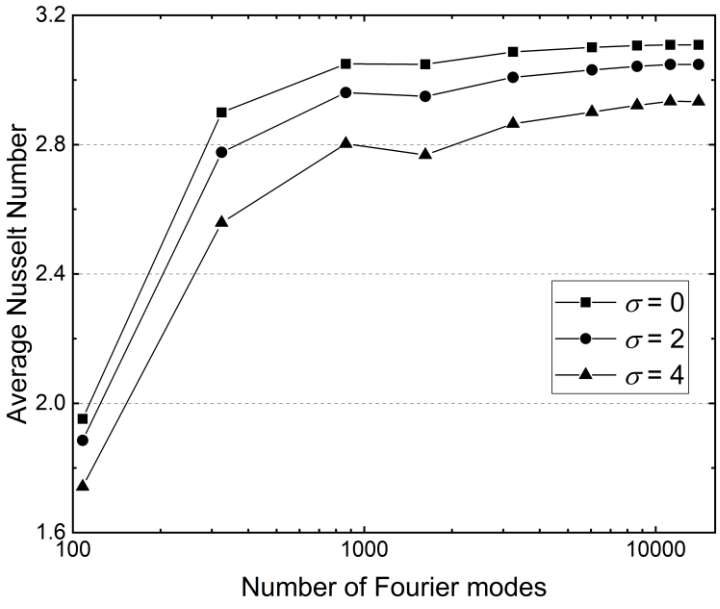

443

444 **Fig. 2.** Example of the convergence of the FS solutions: Variation of the average Nusselt
445 number ($\overline{Nu}$) versus the total number of Fourier modes for the V-het configuration (vertical
446 heterogeneity) at $\overline{Ra}=100$.
447
448 To further verify the FS solutions, a FE analysis is performed for some test cases using
449 COMSOL Multiphysics. We checked relatively simple cases, dealing with $\overline{Ra}=100$ and low
450 rates of heterogeneity ($\sigma=0$ and 2 for the V-het configuration and $\varsigma=0$, 2 for the H-het
451 configuration), in order to facilitate convergence and to avoid numerical artifacts in the FE
452 solutions that could affect the comparisons. A grid dependence test is conducted for each case
453 using different levels of grid refinement in COMSOL. The FE computations are challenging
454 because the gridding effect is important. The mesh-independent solutions have been obtained
455 with a computational mesh of about 80K nodes in the homogeneous cases ($\sigma=0$ or $\varsigma=0$)
456 and 310K nodes for the heterogeneous cases ($\sigma=2$ or $\varsigma=2$). The temperature field at the
457 vertical slice *Y*=0.5 obtained from FS and FE solutions for these test cases are plotted in Fig.
458 3. Table 2 lists the converged results of the average Nusselt number. From Fig. 3 and Table 2,
459 it is observed that FS solutions show excellent agreement with FE solutions at various
460 parameters, which indicates the correctness of the code developed for the FS solutions and
461 gives confidence in the correctness of the developed COMSOL model. It is relevant to
462 mention that while similar accuracy are obtained for these test cases with both solutions, the
463 FS solution is significantly more efficient as it requires fewer degrees of freedom than the FE
464 solution. For instance, in the V-het configuration ($\sigma=2$), the FS solution is obtained with
465 8,640 Fourier modes while the FE solution requires a computational mesh of 310K nodes
466 involving more than 620K degrees of freedom.
467
468 **Table 2.** Comparison between the FS and FE solutions: The average Nusselt number

$\overline{Nu}$	Configuration V-het		Configuration H-het	
	$\sigma=0$	$\sigma=2$	$\varsigma=0$	$\varsigma=2$
FS solution	3.101	3.048	2.474	2.357

FE solution	3.073	2.981	2.456	2.343

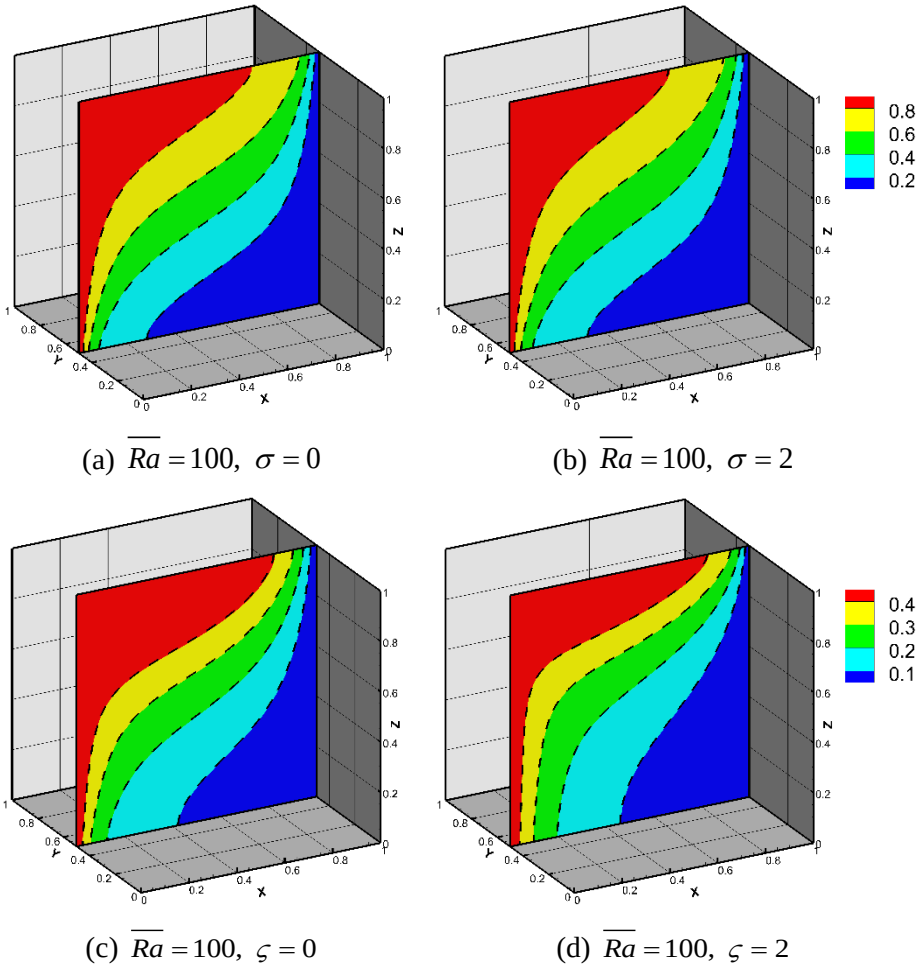

(a) $\overline{Ra}=100,\ \sigma=0$ (b) $\overline{Ra}=100,\ \sigma=2$

(c) $\overline{Ra}=100,\ \varsigma=0$ (d) $\overline{Ra}=100,\ \varsigma=2$

Fig. 3. Comparison between the FS (colored map) and FE (dashed lines) solutions: The main isotherms at the vertical slice Y=0.5 for the configurations V-het (top) and H-het (bottom).

4.2 Reference solutions for code benchmarking: NC and entropy generation

The problem of NC in a porous enclosure is accepted as a common benchmark for numerical codes. Different solutions of this problem have been obtained based on a variety of numerical methods (see Fahs et al. [2015] and reference therein). Comparison between existing solutions is widely used to validate and assess new developed numerical schemes and to help modelers in handling codes interfaces and in data processing. Due to computation limitations, the existing solutions are restricted to 2D. Even in 2D, the numerical accuracy of the entropy generation is not well discussed, which can be significant because it requires a delicate post-

processing procedure based on the reconstruction of thermal and fluid fluxes. Here, taking advantage of the accuracy and performance of the developed FS method, we provide reference solutions that could be useful for benchmarking codes dealing with NC in porous domains and associated entropy generation. The first set of solutions deal with low large-scale Rayleigh number ($\overline{Ra}=10$) with different rates of heterogeneity ($\sigma=0$, 2 and 4 for the V-het configuration and $\varsigma=0$, 2 and 4 for the H-het configuration). These cases are relatively simple from the computational point of view as they deal with a low Rayleigh number. They are useful for codes validations but not appropriate for inter-codes comparison. A relevant benchmark problem for comparing numerical methods should be able to make clear distinctions between the compared methods. Thus, we present solutions for cases dealing with relatively high Rayleigh number and a high rate of heterogeneity. For such cases, it is well-known that numerical schemes may lead to errors with clear grid-based artifacts. Accurate solutions of such cases represent a major challenge for finite-element simulations. Heterogeneity compounds the challenge as an accurate velocity field in heterogenous porous media requires appropriate numerical schemes [Younes et al. 2013]. Thus, we present a second set of solutions for cases dealing with $\overline{Ra}=200$ and $\sigma=0$, 2 and 4 (for the V-het configuration) and $\varsigma=0$, 2 and 4 (for the H-het configuration).

We provide several quantitative indicators related to heat transfer and entropy generation. The quantitative indicators facilitate inter-code comparison as they are more for comparison than visual inspection of isotherms [Prasad and Simmons, 2005]. We use the average Nusselt number as a metric of heat transfer processes, and the total entropy generation as well as the average Bejan numbers to assess entropy generation. All these metrics are calculated without any approximation based on the Fourier series. The results for all test cases are summarized in Table 3. This table provides high-quality data that could be used as references for benchmarking codes dealing with NC and related entropy generation.

Table 3. Quantitative indicators for benchmarking: average Nusselt number ($\overline{Nu}$), total entropy generation number (N_{tot}) and the average Bejan number ($\overline{Be}$).

	Configuration V-het					
	$\overline{Ra}=10$			$\overline{Ra}=200$		
	$\sigma=0$	$\sigma=2$	$\sigma=4$	$\sigma=0$	$\sigma=2$	$\sigma=4$
$\overline{Nu}$	1.079	1.090	1.111	4.936	4.751	4.218
N_{tot}	4.493	4.493	4.529	40.729	39.485	46.349
$\overline{Be}$	0.319	0.356	0.453	0.164	0.166	0.170
	Configuration H-het					
	$\overline{Ra}=10$			$\overline{Ra}=200$		
	$\varsigma=0$	$\varsigma=2$	$\varsigma=4$	$\varsigma=0$	$\varsigma=2$	$\varsigma=4$
$\overline{Nu}$	1.042	1.037	1.027	3.921	3.737	3.295
N_{tot}	2.419	2.238	1.866	21.205	18.949	15.243
$\overline{Be}$	0.316	0.328	0.379	0.151	0.143	0.138

4.3 Effect of large-scale thermal Rayleigh number on NC and entropy generation in heterogeneous domains

The Rayleigh number is the main parameter controlling NC processes. In homogeneous domains, the effect of this number on convective flow, heat fluxes and processes irreversibility is a common topic in literature. In this work, we suggest the use of the large-scale number ($\overline{Ra}$) as the controlling parameter in heterogeneous domain. This section aims at investigating the effect of this new suggested $\overline{Ra}$ on NC and entropy generation in heterogeneous domain. To this end, we analyze the configurations V-het ($\sigma=2$) and H-het ($\varsigma=2$) with varied large-scale Rayleigh numbers ($\overline{Ra}=10$, 100, and 200).

To understand the flow structure, we plot in Fig. 4 the stream-tubes highlighted with the Darcy's vertical velocity component (Q_Z). For the V-het configuration (Figs. 4a-4c), one main convective vortex (torus-like convection cell) occurs in the domain around the central axis of symmetry parallel to the *Y*-axis. The vertical velocity component (color scale) indicates a clockwise rotating flow, as expected (hot water flows up the hot face, *X*=0, and

down the cold face, X=1, with faster velocity near the back face, Y=1, where permeability is the largest). The shape and orientation of the vortex depend on the large-scale Rayleigh number. From this point of view, the latter has a similar effect as the local Rayleigh number in homogeneous domain. While the vortex is centric and axially symmetrical for $\overline{Ra} = 10$, it becomes diagonally-oriented and losses its central orientation when the large-scale Rayleigh number is increased. At a constant heterogeneity rate (σ), the increase of the large-scale Rayleigh number can be interpreted as an increase of permeability everywhere in the domain. Thus, the convective flow becomes faster (notice the colour scale in Figs. 4a, b and c), the thermal boundary around the vertical hot and cold walls shrinks and the zone of high velocity moves down, as it can be observed in Figs. 4b and 4c.

For the H-het configuration (Figs. 4d-4f), the flow structure is complex (recall Fig. 1b that temperature is prescribed as a variable at the X=0 face). The main flow structure has the shape of a convergent-divergent spiral vortex with a curved axis oriented from the vertical plane X=0 to the vertical plane Y=0. The vortex structure of the flow is related to both crossed temperature gradients occurring in the domain. The first gradient is generated by the temperature difference between the hot and cold walls (oriented along the X-axis), while the second gradient is related to the variable temperature imposed at the hot wall (oriented along the Y-axis). As for the V-het configuration, the large-scale Rayleigh number affects the flow structure and mainly the location of the vortex at the vertical plane Y=0. The location of the vortex at the vertical plane X=0 is slightly sensitive to $\overline{Ra}$. This makes sense as the origin of the vortex shape at X=0 is the temperature gradient imposed as a boundary condition and independent on $\overline{Ra}$. For both configurations V-het and H-het, the scales of Q_Z shows a significant acceleration of the rotating flow with the increase of $\overline{Ra}$.

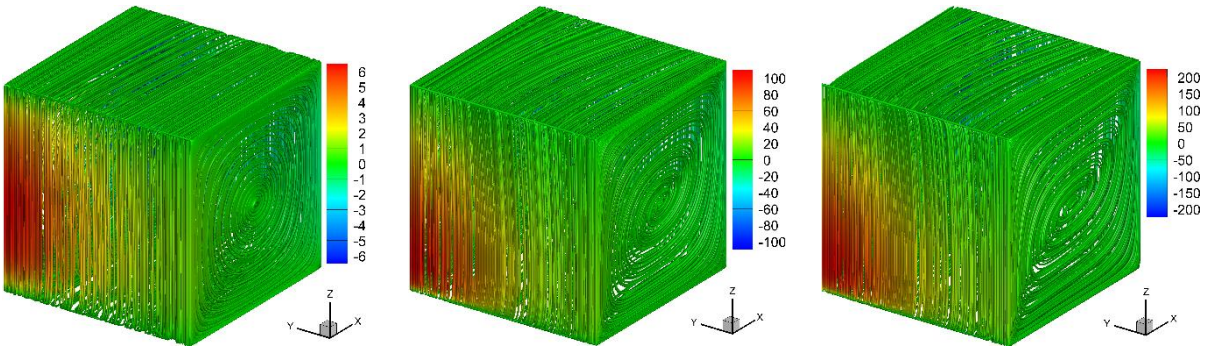

(a) $\overline{Ra}=10$ (b) $\overline{Ra}=100$ (c) $\overline{Ra}=200$

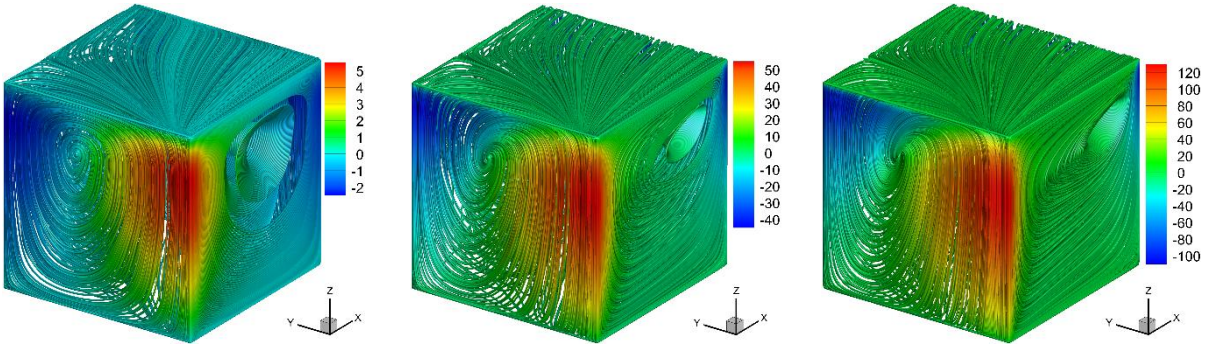

(d) $\overline{Ra}=10$ (e) $\overline{Ra}=100$ (f) $\overline{Ra}=200$

Fig. 4. Effect of large-scale Rayleigh number ($\overline{Ra}$) on convective flow: Stream-tubes highlighted with the vertical velocity component (Q_Z) for the V-het configuration ($\sigma=2$, top) and H-het ($\varsigma=2$, bottom), respectively.

Fig. 5 depicts the isothermal surfaces for each test case. Buoyancy causes the top face to be warmer than the bottom face. However, the two configurations exhibit completely different temperature fields owing to the distinct layouts of heterogeneity and different boundary conditions. At low $\overline{Ra}$, the heat transfer processes are mainly conductive. The isothermal surfaces are almost vertical. With the increase of $\overline{Ra}$, the isothermal surfaces become more distorted inside the enclosure as they follow the flow structure. The transition zone becomes narrower close to the hot boundary (at X=0) because convective heat transfer is enhanced.

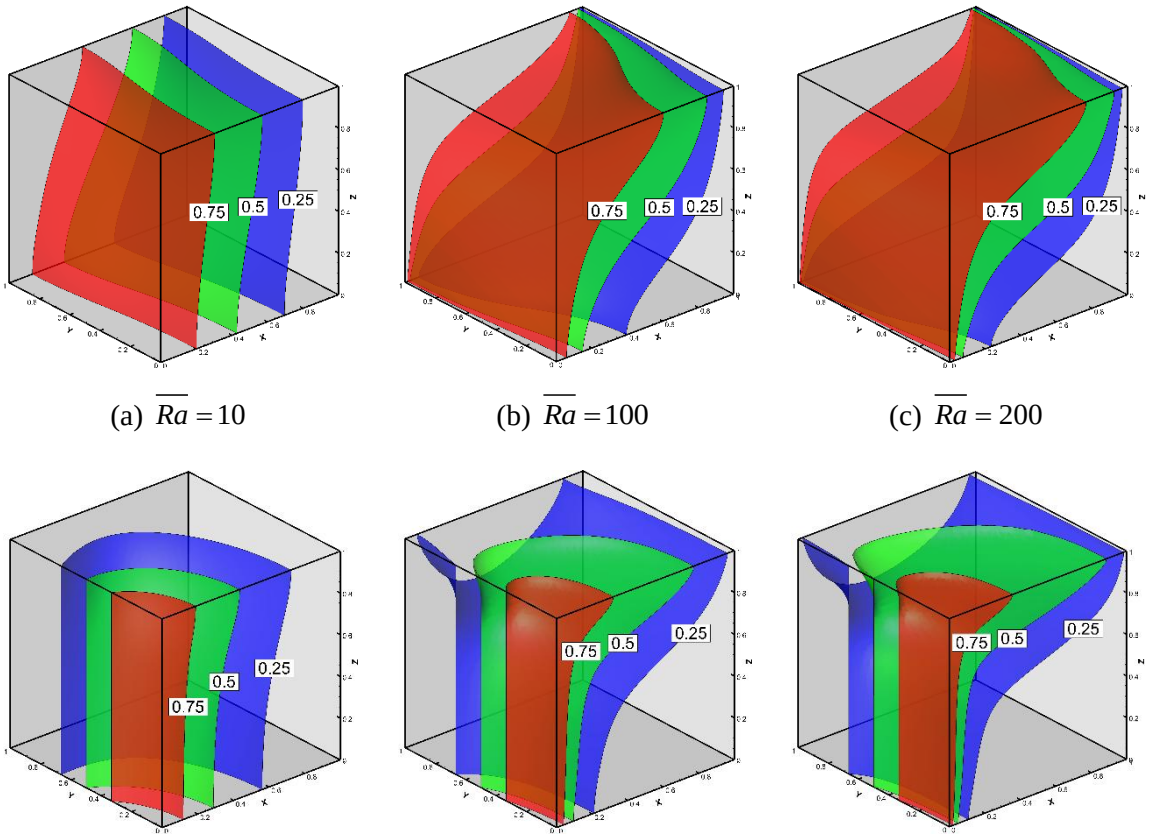

(a) $\overline{Ra}=10$ (b) $\overline{Ra}=100$ (c) $\overline{Ra}=200$

(d) $\overline{Ra}=10$ (e) $\overline{Ra}=100$ (f) $\overline{Ra}=200$

Fig. 5. Effect of large-scale Rayleigh number ($\overline{Ra}$) on temperature distribution: Main temperature iso-surfaces for the configuration V-het ($\sigma=2$, top) and H-het ($\varsigma=2$, bottom), respectively.

The variation of the average Nusselt number with respect to $\overline{Ra}$ is given in Fig. 6a. This figure indicates that $\overline{Nu}$ increases with $\overline{Ra}$, as the buoyancy-induced flow enhances the diffusive heat transfer across the boundary. At the same level of large-scale Rayleigh number and heterogeneity rate, vertical heterogeneity leads to more heat transfer to the domain than horizontal heterogeneity. The space distribution of the heat flux through the hot wall is also investigated using the local Nusselt number as in Figs. 6b and 6c. It is clear that, for the V-het configuration, at a low Rayleigh regime, the heat flux to the domain is uniformly distributed. The increase of $\overline{Ra}$ enhances the heat flux locally in the bottom part of the hot wall (near *Z*=0), particularly in the high permeable zone. The heat flux at the upper part of the wall (near

Z=1) is slightly sensitive to $\overline{Ra}$. For the H-het configuration, we can observe negative local Nusselt numbers, indicating heat losses in some parts of the wall. This is due to the variable temperature imposed at the hot wall. In these parts, due to convective flow in the Y direction (caused by the variable temperature), the temperature of the fluid in the thermal boundary layer becomes higher than the imposed temperature, leading to a heat flux from the domain to the hot wall. The largest heat flux to the domain is observed at the bottom corner (Y=Z=0).

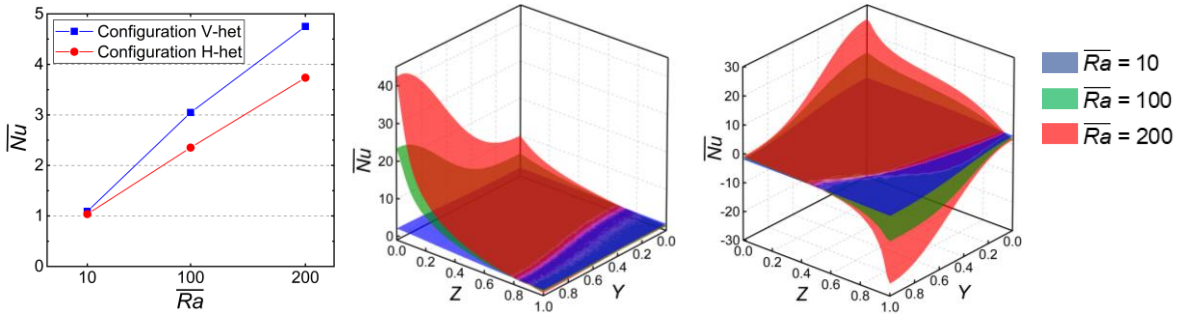

(a) (b) (c)

Fig. 6. Effects of the large-scale Rayleigh number ($\overline{Ra}$) on heat flux through the hot wall: (a) the average Nusselt number, (b) and (c) maps of local Nusselt number of the hot wall for the configurations V-het ($\sigma = 2$) and H-het ($\varsigma = 2$), respectively.

Fig. 7 depicts the local entropy generation number N_E for both configurations V-het and H-het with $\overline{Ra} = 10$, 100, and 200. For the V-het configuration, in the case of low $\overline{Ra}$ (Fig. 7a), two zones of high entropy generation can be observed. The first one is located within the thermal boundary layer near the hot and cold walls, in the high permeable area (toward Y=1). In this zone, the high permeability leads to a high fluid circulation, which causes irreversibility due to viscous dissipation. The fact that the geometry of this high entropy generation zone resembles the geometry of the high-velocity zone (red in Fig. 4) points that viscous dissipation, rather than mixing, is the main entropy generation process. Mixing only displays in enlarging the high entropy generation towards the bottom of the X=0 face, where temperature gradients are highest (see Fig. 5). For low Rayleigh number, a second zone of

high entropy generation is located near the top (Z=1) where velocity is high due to the heterogeneity. This zone is displaced to the back (X=1) when Rayleigh number increases which causes a severe increase in temperature gradients and thus to mixing between hot and cold fluids. The temperature gradient in this zone is relatively high due to mixing. Thus entropy generation in this zone is mainly related to the conduction effect. When $\overline{Ra}$ is increased (Figs. 7b and 7c), the thermal boundary layer shrinks, and the fluid circulation increases. But, overall, entropy generation due to flow dominates, and the maximum local entropy generation appears within the thermal boundary layer near the hot and cold walls at X=0 and X=1 and increases along the Y axis from Y=0 and Y=1, as the gradient of temperature and the velocity field are intensified locally due to the heterogeneity of porous medium. For the H-het configuration, the zone of high entropy generation is located just near the hot wall, in contrast to the V-het configuration where high entropy generation is observed near both hot and cold walls. This is related to the boundary conditions. Near the hot wall, there is a thermal gradient related to the imposed variable temperature and the temperature difference with the cold wall. Thus entropy generation due to heat transfer at the hot side (Y=0) of the hot wall (X=0) is more important than that at the cold wall. Note also that entropy generation is more pronounced at the top surface than at the bottom surface, where permeability is smallest.

Fig.8 depicts the variation of total entropy generation number (N_{tot}), the total mixing rate (N_T), and the average Bejan number ($\overline{Be}$) as a function of the large-scale Rayleigh number. For both configurations, V-het and H-het, the total entropy generation number increases significantly with $\overline{Ra}$, as the higher $\overline{Ra}$ leads to an enhancement of fluid flow and convective heat transfer (Fig. 8a). Also in both configurations, all the average Bejan numbers are far below 0.5, indicating that the irreversibility due to fluid flow makes the major contribution on the total entropy generation. Besides, $\overline{Be}$ decreases with the increase of $\overline{Ra}$.

This indicates that fluid flow irreversibility becomes more significant with the increase of $\overline{Ra}$.

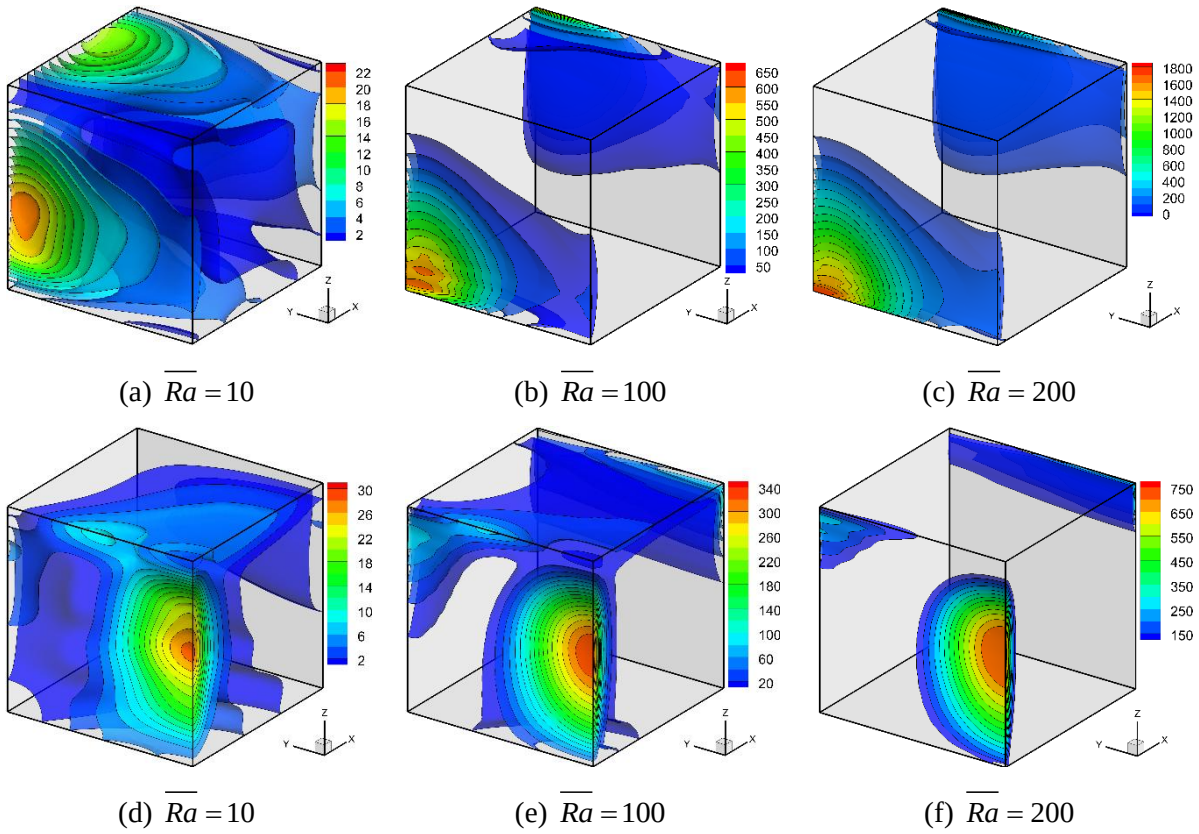

Fig. 7. Effect of large-scale Rayleigh number ($\overline{Ra}$) on entropy generation: Iso-surfaces of local entropy generation number (N_E) for the configuration V-het ($\sigma=2$, top) and H-het ($\varsigma=2$, bottom), respectively.

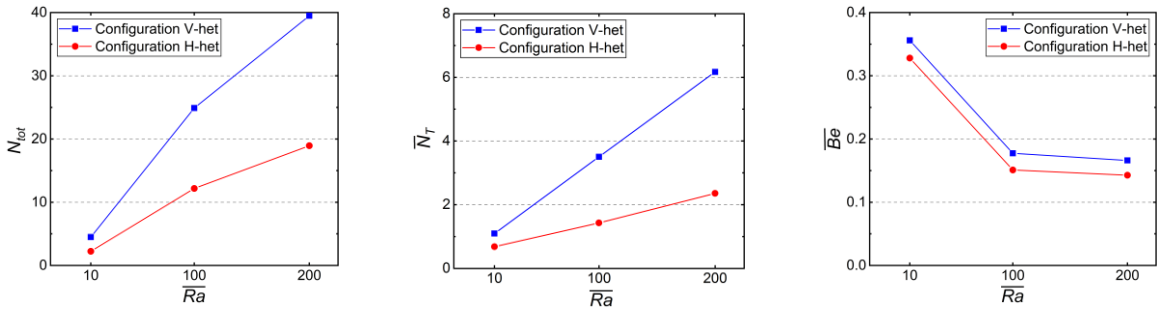

Fig. 8. Effect of large-scale Rayleigh number ($\overline{Ra}$) on entropy generation: The total entropy generation number (N_{tot} , left), the total mixing rate (N_T , center), and the average Bejan number ($\overline{Be}$, right) for the configuration V-het ($\sigma=2$) and H-het ($\varsigma=2$), respectively.

4.4 Influence of heterogeneity

To investigate the effect of varying heterogeneity on the 3D natural convection and entropy generation, we fix the large-scale Rayleigh number at $\overline{Ra} = 100$, and vary the rate of heterogeneity from 0 to 4. Fig. 9 shows the stream-tubes highlighted with the Darcy's vertical velocity component (Q_Z) for the rate of heterogeneity varying from 0 to 4. We recall that, at a constant large-scale Rayleigh number, the increase of the rate of heterogeneity, for the configuration V-het (resp. H-het) corresponds to higher permeability around the vertical plane Y=1 (resp. top surface) and lower permeability near the vertical wall Y=0 (resp. bottom surface), so that the arithmetic average of permeability is the same for the the three rates. For the V-het configuration (Figs. 9a-9c), increasing heterogeneity enhances fluid flow locally and raises the maximum vertical velocity component. The region of maximum Q_Z moves toward the corner near Y=1 as the rate of heterogeneity increases, because increasing heterogeneity induces an increase of the local Rayleigh number near Y=1, and a decrease near Y=0. The flow structure for $\sigma = 0$ (homogeneous case, when the flow structure is 2D) and $\sigma = 2$ are quite similar, except for the increase of vertical flux near Y=1 at the front (X=0) face. However, for the high rate of heterogeneity, we can observe two vortices in the zone of low permeability.

For the H-het configuration (Figs. 9d-9f) the region of maximum velocity moves upward with the increase of the level of heterogeneity, as expected. However, the value of maximum velocity for this configuration is only slightly influenced by the variation of heterogeneity rate. In contrast to the V-het configuration, the flow structure is affected by the rate of heterogeneity, as it can be observed in Figs. 9d-9f, where the location of the vortices at the

planes X=0 and Y=0 are moving towards the high permeable zones when the rate of heterogeneity is increased.

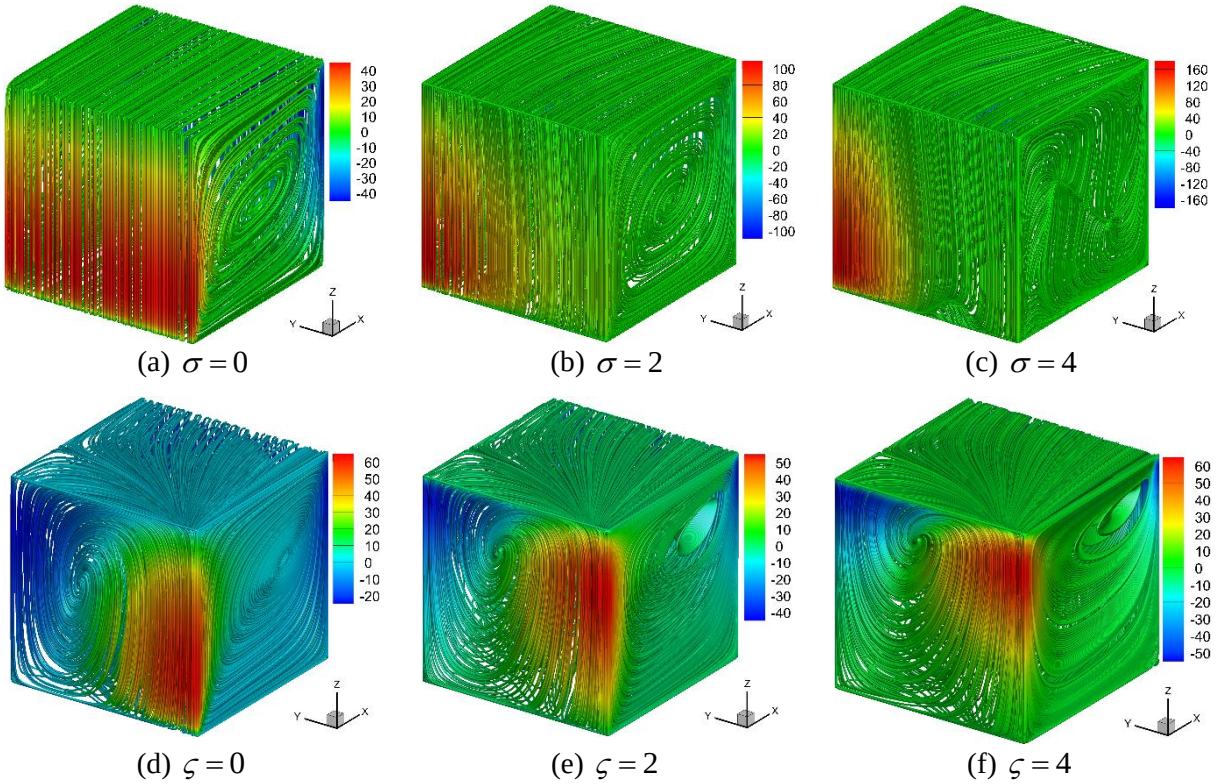

Fig. 9. Effect of heterogeneity on convective flow: Stream-tubes highlighted with the vertical velocity component (Q_Z) for the configuration V-het (top) and H-het (bottom) for $\overline{Ra} = 100$.

The isothermal surfaces for both configurations are plotted in Fig. 10. For the V-het configuration, when the level of heterogeneity is $\sigma = 0$, the porous medium is homogeneous, resulting in a quasi 2D problem. The isothermal surfaces, shown in Fig. 10a, exhibit the 2D nature of heat transfer in the enclosure. As the rate of heterogeneity increases to $\sigma = 2$ and 4 (Figs. 10b and 10c), the isothermal surfaces become increasingly distorted inside the enclosure. The transition zone becomes narrow close to the hot and cold boundaries near Y=1, and wide near Y=0. This is because although the three cases take the same large-scale Rayleigh number, the rising of the rate of heterogeneity leads to an increase of the local Rayleigh number near Y=1, and a decrease of that near Y=0. Basically, the higher local Rayleigh number intensifies the flow velocity and enhances the convective heat transfer in the

vicinity of Y=1. The opposite effect is found near Y=0. Therefore, a correlation between the isothermal surfaces and the rate of heterogeneity is observed for this configuration: the higher the rate of heterogeneity, the more distorted the temperature iso-surfaces. Contrarily, for the H-het configuration (Figs. 10d-10f), the impact of heterogeneity is much less evident influence on the shape of isothermal surfaces. The three cases exhibit a typical 3D nature of heat transfer in the enclosure. Unlike the V-het configuration, the 3D effect for the H-het configuration originates from the varying temperature boundary condition, rather than heterogeneity. Increase of rate of heterogeneity only causes a slight change in the shape of isotherms in the bottom half of the X=0, Y=0 edge, where the transition zone becomes wider due to the decrease of local Rayleigh number that reduces the convective heat transfer at this region.

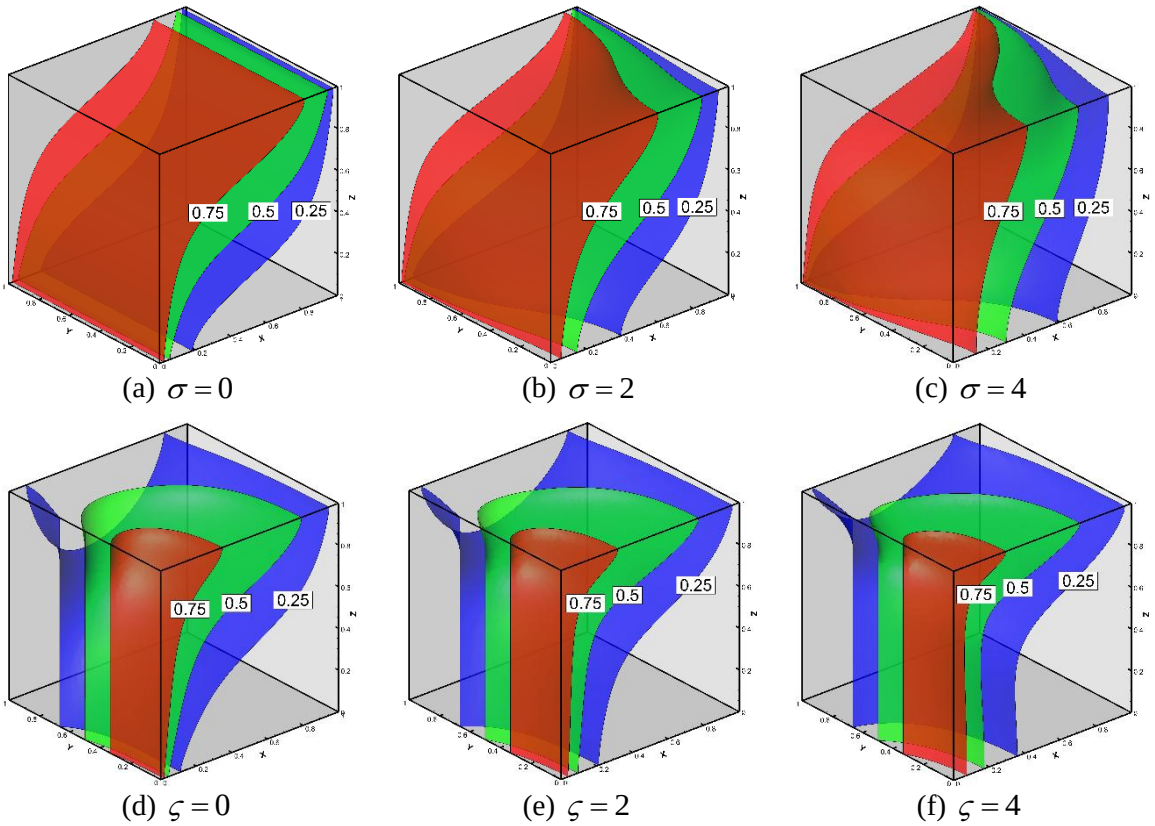

(a) $\sigma = 0$ (b) $\sigma = 2$ (c) $\sigma = 4$

(d) $\varsigma = 0$ (e) $\varsigma = 2$ (f) $\varsigma = 4$

Fig. 10. Effect of heterogeneity on temperature distribution: Main temperature iso-surfaces for the configuration V-het (top) and H-het (bottom) for $\overline{Ra} = 100$.

The effect of heterogeneity on the heat flux through the hot wall is shown in Fig. 11, which displays the variation of the average Nusselt number ($\overline{Nu}$) as a function of the rate of heterogeneity (σ for the V-het configuration and ς for the H-het configuration) for two different values of large-scale Rayleigh number. The results show that in both configurations, the average heat flux to the domain decreases with the increase of the rate of heterogeneity. The effect of rate of heterogeneity on the heat flux is more significant at high Rayleigh regimes, which highlights that the reduction of heat thermal gradients in low permeability zones is slightly more relevant than their increase in regions of high permeability. The reduction is not large, but relevant for a proper understanding of entropy generation dependence on heterogeneity.

The spatial variations of the local Nusselt number on the hot wall for configurations V-het and H-het are depicted in Figs. 11b and 11c, respectively. For the V-het configuration, the increase of the rate of heterogeneity enhances the heat flux to the domain at the high permeable zone and reduces it in the low permeable zone. The opposite is true in the H-het configuration, where the maximum local Nusselt number can be observed in the zone of low permeability.

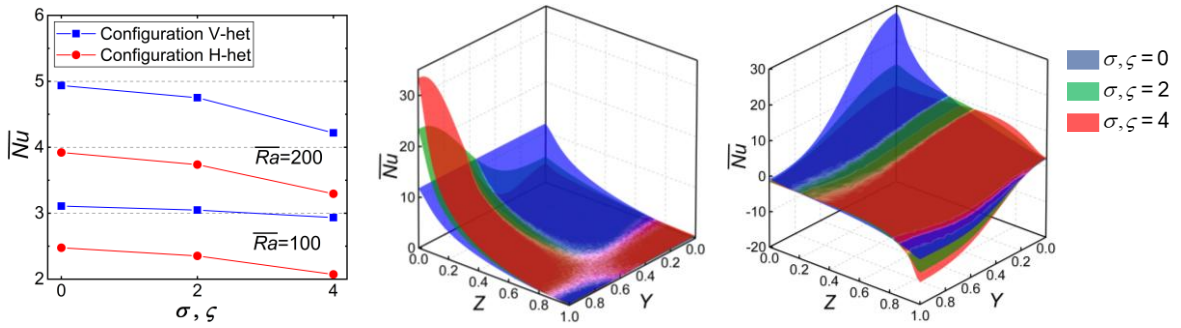

(a) (b) (c)

Fig. 11. Effect of heterogeneity on heat flux through the hot wall: (a) the average Nusselt number, (b) and (c) maps of local Nusselt number of the hot wall for the configurations V-het and H-het with $\overline{Ra} = 100$, respectively.

Fig. 12 depicts the local entropy generation number N_E for both configurations with varying rate of heterogeneity. The 2D nature of the homogeneous ($\sigma = 0$) V-het configuration also shows on the local entropy generation, which does not change along the *Y* axis (Fig. 12a). As the rate of heterogeneity increases, the local entropy generation varies along the *Y* axis. Specifically, the zone of maximum local entropy generation moves toward the corner in the vicinity of *Y*=1, where the local Rayleigh number near *Y*=1, which intensifies both the temperature gradient (Figs. 10a, b, and c) and the fluid flux (Figs. 9a, b, and c). Both increases trigger an increase on the maximum local entropy generation. For the H-het configuration (Figs. 12d-12f), a negative correlation between the heterogeneity rate and the maximum local entropy generation is found: the higher the rate of heterogeneity, the smaller the maximum value of local entropy generation (see the color scale). It should be noted that the effect of the heterogeneity rate on the maximum value of local entropy generation is not very evident for this configuration. This is because for the H-het configuration, neither the temperature gradient nor the maximum velocity change much with the variation of heterogeneity rate (see Figs. 9 and 10). In the vicinity of hot wall at *X*=0, the zone of maximum local entropy generation moves upward with the increase of heterogeneity rate, which is consistent with the velocity field (Fig. 9), as the higher heterogeneity rate increases the local Rayleigh number near *Z*=1 and decreases that near *Z*=0, which further influences the fluid flow and modifies the distribution of local entropy generation. It may be noticed, however, that the maximum entropy generation occurs slightly below the maximum velocity, which reflects that thermal gradients are highest in the lower part (Fig. 10) and contribute to the mixing term of entropy generation.

Fig. 13 depicts the variation of the total entropy generation number (N_{tot}), the total mixing rate (N_T), and the average Bejan number ($\overline{Be}$) as a function of the rate of heterogeneity. The most important observation is that both total entropy generation and mixing rate are

virtually insensitive to heterogeneity, which implies that the adopted effective permeability is indeed appropriate. The total entropy generation number decreases slightly as the heterogeneity level increases for both configurations, which is probably due to the shrink of the active zone for local entropy generation. This phenomenon is also observed in Fig. 9, where the flow velocity field shows similar profiles. N_{tot} slightly decreases with the increase of the rate of heterogeneity. The average Bejan number demonstrates that the irreversibility due to fluid flow has a dominant influence on the total entropy generation in the domain. Similar to the total entropy generation number, in the H-het configuration, $\overline{Be}$ decreases with the increase of the rate of heterogeneity. In the opposite, for the V-het configuration, $\overline{Be}$ significantly increases with the increase of the rate of heterogeneity.

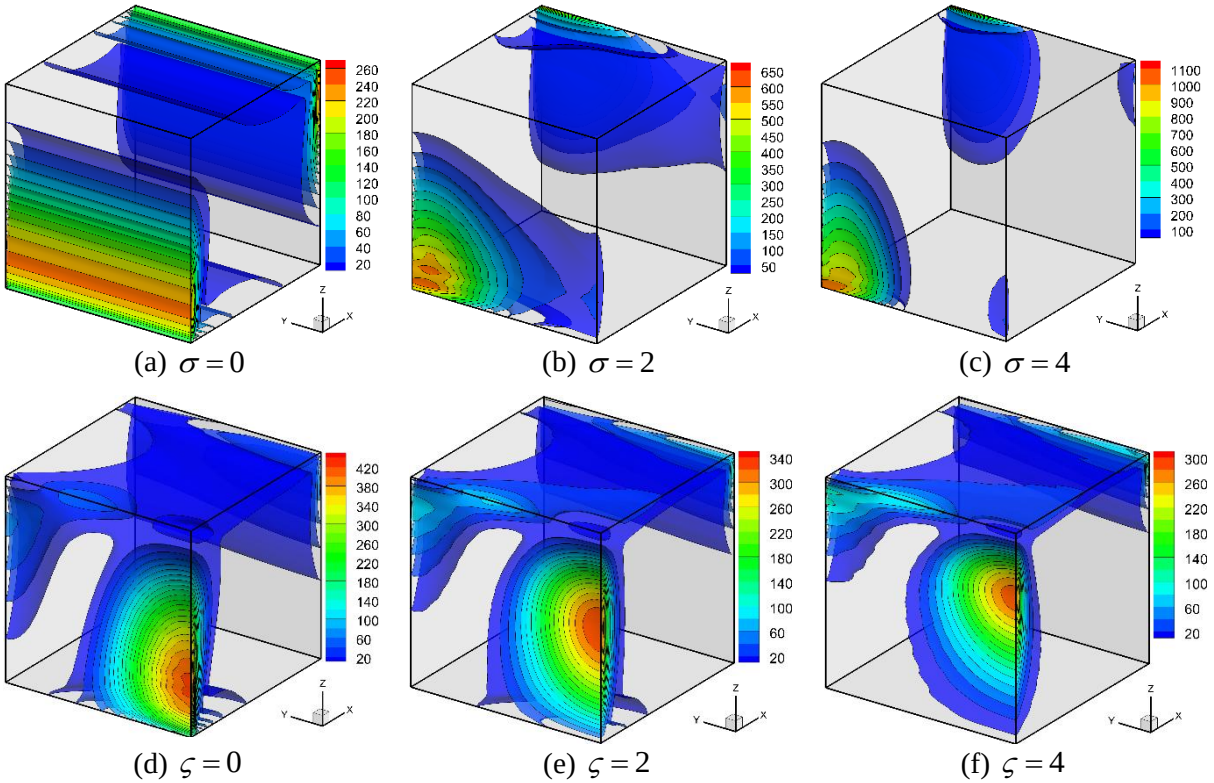

(a) $\sigma = 0$ (b) $\sigma = 2$ (c) $\sigma = 4$

(d) $\varsigma = 0$ (e) $\varsigma = 2$ (f) $\varsigma = 4$

Fig. 12. Effect of heterogeneity on entropy generation: Iso-surfaces of local entropy generation number (N_E) for the V-het configuration (top) and H-het (bottom) for $\overline{Ra} = 100$.

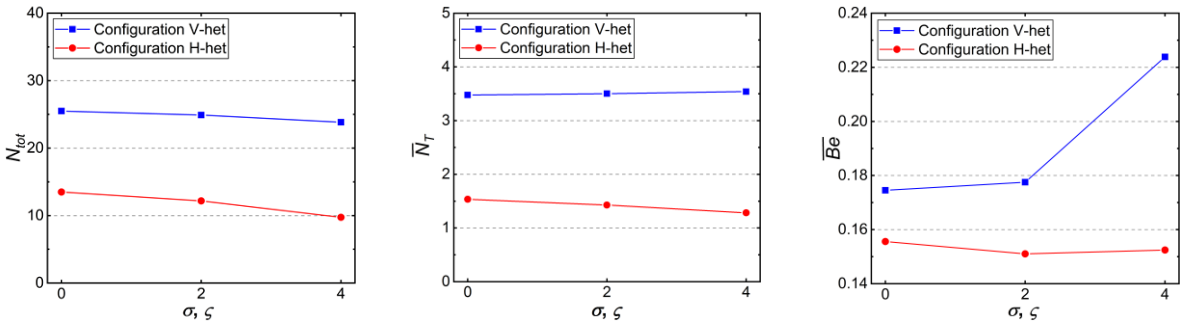

Fig. 13. Effect of heterogeneity on entropy generation: The total entropy generation number (N_{tot}, left), the total mixing rate (N_T, center), and the average Bejan number ($\overline{Be}$, right) for the configurations V-het and H-het ($\overline{Ra}=100$).

4.5 Third dimension effect

The goal of this section is to evaluate the effect of the third dimension on the convective flow, heat transfer, and entropy generation. Thus, we compare the 3D results with those of equivalent 2D models. For the V-het configuration, the third dimension effects are caused by heterogeneity. Hence, in the equivalent 2D model, we consider a homogenous domain with equivalent permeability as defined in the large-scale Rayleigh number (Eq. (41)). Under this assumption, the 3D model can be simplified to 2D. For the H-het configuration, the third dimension effects are related to the variable boundary conditions. Thus, in the equivalent 2D model, we keep the heterogeneity but we assume a constant temperature on the hot wall which is equal to the average temperature ($\vartheta=\int_0^1 f(Y)dY=0.5$). For the sake of brevity, we do not consider spatial maps of temperature and entropy generation, but just compare the 2D and 3D results in terms of the average Nusselt number as metric of heat transfer, the total entropy number, and the dimensionless mixing rate (as metrics of entropy generation), and the dimensionless temperature at the top center point (X=0.5, Y=0.5, Z=1 for 3D cases, and X=0.5, Z=1 for 2D cases).

Fig 14 depicts the variation of these metrics with respect to the large-scale Rayleigh number for both 2D and 3D models with varying rates of heterogeneity for V-het configuration.

Obviously, 2D results insensitive to heterogeneity because the V-het 2D model is homogeneous and identical to the 3D model with $\sigma = 0$. Therefore, the 3D effect is similar to the effect of heterogeneity discussed in the previous section. Therefore, the 2D assumption leads to an overestimation of the heat losses and average Nusselt number (Fig. 14a). But the impact is small in terms of both total entropy generation and mixing rate (Figs. 14b and c). The discrepancy between 2D and 3D models is more significant at high Rayleigh regimes. As the 3D effects are caused by the heterogeneity, it is clear in Fig.14 that the increase of the rate of heterogeneity enlarges the discrepancy between 2D and 3D models.

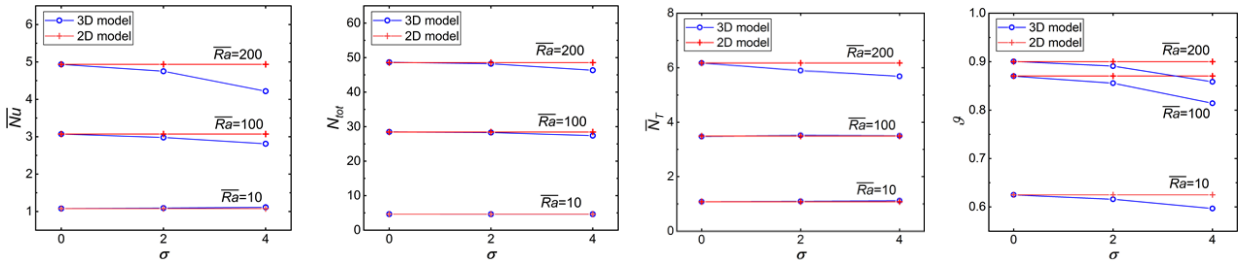

Fig. 14. Third dimension effect on the (a) average Nusselt number, (b) total entropy generation number, (c) the dimensionless mixing rate, and (c) temperature at the top center point for the V-het configuration.

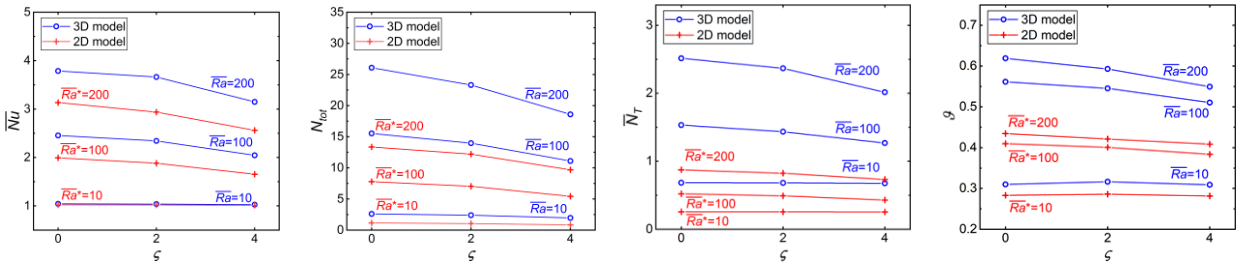

Fig. 15. Third dimension effect on the (a) average Nusselt number, (b) total entropy generation number, (c) dimensionless mixing rate, and (d) temperature at the top center point for the configuration H-het.

The H-het configuration yields more interesting results than V-het. The 2D model largely underestimates all indicators (Fig. 15). Simplifying to 2D (i.e., neglecting temperature variability in the hot face of the enclosure) reduces somewhat the heat flux (Nusselt number, Fig. 15a) and leads to a more homogeneous flow and temperature distribution. Lack of variability leads to a dramatic reduction in total entropy generation (a factor around 2, Fig.

15b) and even more in mixing rate (a factor around 3, Fig. 15c). The absolute value of the discrepancy between 2D and 3D simulations is more significant at high Rayleigh numbers. A hint on the reason for the discrepancy can be gained from the temperature at the middle of the top face (Fig. 15d). High permeability at the top causes active fluid circulation, so that temperature at the top face approaches asymptotically the temperature of the hot face (0.5 in the 2D case) as the Rayleigh number increases. However, circulation is most active near the hot end of this face in the 3D case (recall Fig. 9). As a result, temperature at the middle of the top face is above the average temperature of the hot face (Fig. 15d), which explains the large increase in the mixing rate.

5 Conclusions

In this work, we investigate three-dimensional natural convection and associated entropy generation in heterogeneous porous media under steady-state conditions. Two typical configurations are considered: one has vertically stratified porous media and subject to constant temperature boundary conditions, the other has horizontally stratified porous media and subject to spatially varying temperature boundary conditions. Both configurations lead to three-dimensional flow conditions that cannot be simplified to two-dimensions. The 3D effect of the first configuration comes from the heterogeneity in permeability, while that of the second configuration originates from the varying temperature boundary conditions. As 3D simulations are computationally expensive, the Fourier series (FS) method is used to obtain highly accurate solutions in affordable CPU time. The comparison between the FS and finite element methods (COMSOL) confirms the validity of the new developed FS solutions, which provide a highly accurate three-dimensional benchmark for testing numerical codes.

The solution is different for each configuration. In the V-het configuration, the typical convection cell of 2D natural convection increases its vorticity and splits into two vortices as

heterogeneity increases. In the H-het configuration, the variable temperature of the hot face causes the vortex to curve into a quarter of a torus whose axis displaces upwards as heterogeneity increases. Comparison between 2D and 3D simulations shows that the 2D assumption underestimates the heat flux to the domain, the entropy generation and the temperature on the top surface. The underestimation is dramatic in the horizontally stratified case.

We propose an effective large-scale Rayleigh number to characterize natural convection in heterogeneous media. This new large-scale Rayleigh number is similar to the standard Rayleigh number for homogeneous media, but using the arithmetic average of the heterogeneous permeability. Based on the FS solutions, we investigate the effect of this effective Rayleigh number and level of heterogeneity on heat and fluid flux, as quantified by the Nusselt number (dimensionless heat flux) and entropy generation (both from viscous dissipation and mixing). Results reveal that, as expected, the increase of the effective Rayleigh number considerably intensifies the fluid flow and enhances the convective heat transfer, inducing high-temperature gradients and large local entropy generation near the boundaries and, thus, within the enclosure. These increases lead to a large increase of total entropy generation, in terms of both viscous forces dissipation and mixing rate.

Perhaps more surprisingly, we find a very mild but negative correlation between the heterogeneity rate and entropy generation for both configurations. In fact, both total entropy and, especially, mixing rate remain virtually constant, despite a reduction of heat flux (Nusselt number) when heterogeneity increases. This is important because it suggests that the proposed Rayleigh number is indeed sufficient to explain the impact of heterogeneity on dissipative processes and dissolution/precipitation reactions in cases where density variations are driven by changes in composition, so that mixing controls reaction rates (such as in CO_2 dissolution in carbon storage problems). But it is surprising for two reasons. First, for a given effective

permeability, one would expect both fluxes and temperature (concentration) gradients to increase with heterogeneity. Second, the arithmetic average is the largest of all reasonable averages (in fact, it is the effective permeability only for ideal infinite dimension geometries), so that one would expect other more traditional averages (e.g., geometric or 1/3 power averaging) to work better. We conclude that the explanation lies in this double paradox. Had we chosen any other average for permeability and large-scale Rayleigh number, we would have found that, indeed, entropy generation increases with heterogeneity when the Rayleigh number is fixed. Further, as the heat (solute mass) flux drops when increasing heterogeneity while fixing Rayleigh number, the expectation of increased disorder turns out to be correct for a fixed boundary heat (solute mass) flux. In summary, the proposed Rayleigh number would not be appropriate for predicting boundary fluxes, which might require using the traditional effective permeability, but it is excellent in predicting entropy generation indicators, which become virtually insensitive to heterogeneity.

Acknowledgement

This work has been supported by the National Natural Science Foundation of China (Grant No. 11702199). The data used in this work are available on the GitHub repository: https://github.com/fahs-LHYGES.

References

[1] A.M.J. Al-Zamily, Analysis of natural convection and entropy generation in a cavity filled with multi-layers of porous medium and nanofluid with a heat generation, International Journal of Heat and Mass Transfer. 106 (2017) 1218–1231. https://doi.org/10.1016/j.ijheatmasstransfer.2016.10.102.

[2] T. Basak, P. Gunda, R. Anandalakshmi, Analysis of entropy generation during natural convection in porous right-angled triangular cavities with various thermal boundary conditions, International Journal of Heat and Mass Transfer. 55 (2012) 4521–4535. https://doi.org/10.1016/j.ijheatmasstransfer.2012.03.061.

[3] T. Basak, R.S. Kaluri, A.R. Balakrishnan, Entropy Generation During Natural Convection in a Porous Cavity: Effect of Thermal Boundary Conditions, Numerical Heat Transfer, Part A: Applications. 62 (2012) 336–364. https://doi.org/10.1080/10407782.2012.691059.

[4] A.C. Baytaş, Entropy generation for natural convection in an inclined porous cavity, International Journal of Heat and Mass Transfer. 43 (2000) 2089–2099. https://doi.org/10.1016/S0017-9310(99)00291-4.

[5] A.C. Baytas, Entropy Generation for Thermal Nonequilibrium Natural Convection with a Non-Darcy Flow Model in a Porous Enclosure Filled with a Heat-Generating Solid Phase, J Por Media. 10 (2007) 261–275. https://doi.org/10.1615/JPorMedia.v10.i3.30.

[6] T. Le Borgne, M. Dentz, D. Bolster, J. Carrera, J.-R. de Dreuzy, P. Davy, Non-Fickian mixing: Temporal evolution of the scalar dissipation rate in heterogeneous porous media, Advances in Water Resources. 33 (2010) 1468–1475. https://doi.org/10.1016/j.advwatres.2010.08.006.

[7] M. Bouabid, M. Magherbi, N. Hidouri, A.B. Brahim, Entropy Generation at Natural Convection in an Inclined Rectangular Cavity, Entropy. 13 (2011) 1020–1033. https://doi.org/10.3390/e13051020.

[8] A. Chamkha, F. Selimefendigil, MHD Free Convection and Entropy Generation in a Corrugated Cavity Filled with a Porous Medium Saturated with Nanofluids, Entropy. 20 (2018) 846. https://doi.org/10.3390/e20110846.

[9] G. Chandra Pal, N. Goswami, S. Pati, Numerical investigation of unsteady natural convection heat transfer and entropy generation from a pair of cylinders in a porous enclosure, Numerical Heat Transfer, Part A: Applications. 74 (2018) 1323–1341. https://doi.org/10.1080/10407782.2018.1507887.

[10] O.A. Cirpka, A.J. Valocchi, Two-dimensional concentration distribution for mixing-controlled bioreactive transport in steady state, Advances in Water Resources. 30 (2007) 1668–1679. https://doi.org/10.1016/j.advwatres.2006.05.022.

[11] P. Datta, P.S. Mahapatra, K. Ghosh, N.K. Manna, S. Sen, Heat Transfer and Entropy Generation in a Porous Square Enclosure in Presence of an Adiabatic Block, Transp Porous Med. 111 (2016) 305–329. https://doi.org/10.1007/s11242-015-0595-5.

[12] M. De Simoni, J. Carrera, X. Sánchez-Vila, A. Guadagnini, A procedure for the solution of multicomponent reactive transport problems, Water Resour. Res. 41 (2005). https://doi.org/10.1029/2005WR004056.

[13] N. Fajraoui, M. Fahs, A. Younes, B. Sudret, Analyzing natural convection in porous enclosure with polynomial chaos expansions: Effect of thermal dispersion, anisotropic permeability and heterogeneity, International Journal of Heat and Mass Transfer. 115 (2017) 205–224. https://doi.org/10.1016/j.ijheatmasstransfer.2017.07.003.

[14] M. Fahs, A. Younes, A. Makradi, A Reference Benchmark Solution for Free Convection in A Square Cavity Filled with A Heterogeneous Porous Medium, Numerical Heat Transfer, Part B: Fundamentals. 67 (2015) 437–462.

https://doi.org/10.1080/10407790.2014.977183.
[15] K. Ghachem, L. Kolsi, C. Mâatki, A.K. Hussein, M.N. Borjini, Numerical simulation of three-dimensional double diffusive free convection flow and irreversibility studies in a solar distiller, International Communications in Heat and Mass Transfer. 39 (2012) 869–876. https://doi.org/10.1016/j.icheatmasstransfer.2012.04.010.
[16] K. Ghasemi, M. Siavashi, MHD nanofluid free convection and entropy generation in porous enclosures with different conductivity ratios, Journal of Magnetism and Magnetic Materials. 442 (2017) 474–490. https://doi.org/10.1016/j.jmmm.2017.07.028.
[17] F.J. Guerrero-Martínez, P.L. Younger, N. Karimi, Three-dimensional numerical modeling of free convection in sloping porous enclosures, International Journal of Heat and Mass Transfer. 98 (2016) 257–267. https://doi.org/10.1016/j.ijheatmasstransfer.2016.03.029.
[18] J.J. Hidalgo, J. Fe, L. Cueto-Felgueroso, R. Juanes, Scaling of Convective Mixing in Porous Media, Phys. Rev. Lett. 109 (2012) 264503. https://doi.org/10.1103/PhysRevLett.109.264503.
[19] J.J. Hidalgo, J. Carrera, Effect of dispersion on the onset of convection during CO_2 sequestration, J. Fluid Mech. 640 (2009) 441–452. https://doi.org/10.1017/S0022112009991480.
[20] S. Hussain, K. Mehmood, M. Sagheer, M. Yamin, Numerical simulation of double diffusive mixed convective nanofluid flow and entropy generation in a square porous enclosure, International Journal of Heat and Mass Transfer. 122 (2018) 1283–1297. https://doi.org/10.1016/j.ijheatmasstransfer.2018.02.082.
[21] IMSL® Fortran Math Library, 2014. https://docs.roguewave.com/imsl/fortran/7.1/html/fnlmath/index.html.
[22] D.B. Ingham, L. Pop, Transport Phenomena in Porous Media III., Elsevier, Burlington, 2005. http://public.ebookcentral.proquest.com/choice/publicfullrecord.aspx?p=318117 (accessed May 25, 2020).
[23] A. Jbara, K. Slimi, A. Mhimid, Entropy generation for unsteady natural convection and thermal radiation inside a porous enclosure, IJEX. 12 (2013) 522. https://doi.org/10.1504/IJEX.2013.055078.
[24] X.-W. Jiang, L. Wan, M.B. Cardenas, S. Ge, X.-S. Wang, Simultaneous rejuvenation and aging of groundwater in basins due to depth-decaying hydraulic conductivity and porosity:, Geophys. Res. Lett. 37 (2010) n/a-n/a. https://doi.org/10.1029/2010GL042387.
[25] R.S. Kaluri, T. Basak, Entropy generation due to natural convection in discretely heated porous square cavities, Energy. 36 (2011) 5065–5080. https://doi.org/10.1016/j.energy.2011.06.001.
[26] Gh.R. Kefayati, Simulation of double diffusive natural convection and entropy generation of power-law fluids in an inclined porous cavity with Soret and Dufour effects (Part I: Study of fluid flow, heat and mass transfer), International Journal of Heat and Mass Transfer. 94 (2016) 539–581. https://doi.org/10.1016/j.ijheatmasstransfer.2015.11.044.
[27] W.A. Khan, R.S.R. Gorla, Entropy Generation in Non-Newtonian Fluids Along Horizontal Plate in Porous Media, Journal of Thermophysics and Heat Transfer. 25 (2011) 298–303. https://doi.org/10.2514/1.51200.
[28] S. Kimura, T. Kiwata, A. Okajima, I. Pop, Conjugate natural convection in porous media, Advances in Water Resources. 20 (1997) 111–126. https://doi.org/10.1016/S0309-1708(96)00025-5.
[29] M.A. Mansour, S.E. Ahmed, A.J. Chamkha, Entropy generation optimization for MHD natural convection of a nanofluid in porous media-filled enclosure with active parts and viscous dissipation, Int Jnl of Num Meth for HFF. 27 (2017) 379–399.

https://doi.org/10.1108/HFF-10-2015-0408.
[30] R.L. Marvel, F.C. Lai, Natural Convection From a Porous Cavity With Sublayers of Nonuniform Thickness: A Lumped System Analysis, Journal of Heat Transfer. 132 (2010) 032602. https://doi.org/10.1115/1.3213527.
[31] A. Mchirgui, N. Hidouri, M. Magherbi, A. Ben Brahim, Second law analysis in double diffusive convection through an inclined porous cavity, Computers & Fluids. 96 (2014) 105–115. https://doi.org/10.1016/j.compfluid.2014.03.008.
[32] I.V. Miroshnichenko, M.A. Sheremet, H.F. Oztop, N. Abu-Hamdeh, Natural convection of alumina-water nanofluid in an open cavity having multiple porous layers, International Journal of Heat and Mass Transfer. 125 (2018) 648–657. https://doi.org/10.1016/j.ijheatmasstransfer.2018.04.108.
[33] V.T. Nguyen, T. Graf, C.R. Guevara Morel, Free thermal convection in heterogeneous porous media, Geothermics. 64 (2016) 152–162. https://doi.org/10.1016/j.geothermics.2016.05.006.
[34] D.A. Nield, A.V. Kuznetsov, The effect of combined vertical and horizontal heterogeneity on the onset of convection in a bidisperse porous medium, International Journal of Heat and Mass Transfer. 50 (2007) 3329–3339. https://doi.org/10.1016/j.ijheatmasstransfer.2007.01.027.
[35] D.A. Nield, A.V. Kuznetsov, The effects of combined horizontal and vertical heterogeneity and anisotropy on the onset of convection in a porous medium, International Journal of Thermal Sciences. 46 (2007) 1211–1218. https://doi.org/10.1016/j.ijthermalsci.2007.01.005.
[36] D.A. Nield, C.T. Simmons, A discussion on the effect of heterogeneity on the onset of convection in a porous medium, Transp Porous Med. 68 (2007) 413–421. https://doi.org/10.1007/s11242-006-9045-8.
[37] D.A. Nield, General Heterogeneity Effects on the Onset of Convection in a Porous Medium, in: P. Vadász (Ed.), Emerging Topics in Heat and Mass Transfer in Porous Media, Springer Netherlands, Dordrecht, 2008: pp. 63–84. https://doi.org/10.1007/978-1-4020-8178-1_3.
[38] D.A. Nield, A.V. Kuznetsov, The effects of combined horizontal and vertical heterogeneity on the onset of convection in a porous medium: Moderate heterogeneity, International Journal of Heat and Mass Transfer. 51 (2008) 2361–2367. https://doi.org/10.1016/j.ijheatmasstransfer.2007.08.011.
[39] D.A. Nield, A.V. Kuznetsov, C.T. Simmons, The Effect of Strong Heterogeneity on the Onset of Convection in a Porous Medium: Non-periodic Global Variation, Transp Porous Med. 77 (2009) 169–186. https://doi.org/10.1007/s11242-008-9297-6.
[40] D.A. Nield, A.V. Kuznetsov, The effects of combined horizontal and vertical heterogeneity on the onset of convection in a porous medium with horizontal throughflow, International Journal of Heat and Mass Transfer. 54 (2011) 5595–5601. https://doi.org/10.1016/j.ijheatmasstransfer.2011.07.019.
[41] D.A. Nield, A.V. Kuznetsov, Local thermal non-equilibrium and heterogeneity effects on the onset of convection in a layered porous medium with vertical throughflow, J Por Media. 18 (2015) 125–136. https://doi.org/10.1615/JPorMedia.v18.i2.40.
[42] D.A. Nield, A. Bejan, Convection in Porous Media, Springer International Publishing, Cham, 2017. https://doi.org/10.1007/978-3-319-49562-0
[43] D.A. Nield, A.V. Kuznetsov, A. Barletta, M. Celli, The Onset of Convection in a Sloping Layered Porous Medium: Effects of Local Thermal Non-equilibrium and Heterogeneity, Transp Porous Med. 114 (2016) 87–97. https://doi.org/10.1007/s11242-016-0728-5.
[44] D.A. Nield, C.T. Simmons, A Brief Introduction to Convection in Porous Media, Transp

Porous Med. 130 (2019) 237–250. https://doi.org/10.1007/s11242-018-1163-6.
[45] B. Noetinger, The effective permeability of a heterogeneous porous medium, Transp Porous Med. 15 (1994) 99–127. https://doi.org/10.1007/BF00625512.
[46] H.F. Oztop, K. Al-Salem, A review on entropy generation in natural and mixed convection heat transfer for energy systems, Renewable and Sustainable Energy Reviews. 16 (2012) 911–920. https://doi.org/10.1016/j.rser.2011.09.012.
[47] G.S.H. Pau, J.B. Bell, K. Pruess, A.S. Almgren, M.J. Lijewski, K. Zhang, High-resolution simulation and characterization of density-driven flow in CO2 storage in saline aquifers, Advances in Water Resources. 33 (2010) 443–455. https://doi.org/10.1016/j.advwatres.2010.01.009.
[48] R. Peyret, Spectral Methods for Incompressible Viscous Flow, Springer New York, New York, NY, 2002. https://doi.org/10.1007/978-1-4757-6557-1.
[49] A. Prasad, C.T. Simmons, Using quantitative indicators to evaluate results from variable-density groundwater flow models, Hydrogeol J. 13 (2005) 905–914. https://doi.org/10.1007/s10040-004-0338-0.
[50] Ph. Renard, G. de Marsily, Calculating equivalent permeability: a review, Advances in Water Resources. 20 (1997) 253–278. https://doi.org/10.1016/S0309-1708(96)00050-4.
[51] M. Rezaei, E. Sanz, E. Raeisi, C. Ayora, E. Vázquez-Suñé, J. Carrera, Reactive transport modeling of calcite dissolution in the fresh-salt water mixing zone, Journal of Hydrology. 311 (2005) 282–298. https://doi.org/10.1016/j.jhydrol.2004.12.017.
[52] A. Riaz, M. Hesse, H.A. Tchelepi, F.M. Orr, Onset of convection in a gravitationally unstable diffusive boundary layer in porous media, J. Fluid Mech. 548 (2006) 87. https://doi.org/10.1017/S0022112005007494.
[53] X. Sanchez-Vila, A. Guadagnini, J. Carrera, Representative hydraulic conductivities in saturated groundwater flow, Rev. Geophys. 44 (2006) RG3002. https://doi.org/10.1029/2005RG000169.
[54] Q. Shao, M. Fahs, H. Hoteit, J. Carrera, P. Ackerer, A. Younes, A 3- D Semianalytical Solution for Density- Driven Flow in Porous Media, Water Resour. Res. 54 (2018). https://doi.org/10.1029/2018WR023583.
[55] C.T. Simmons, A.V. Kuznetsov, D.A. Nield, Effect of strong heterogeneity on the onset of convection in a porous medium: Importance of spatial dimensionality and geologic controls, Water Resour. Res. 46 (2010). https://doi.org/10.1029/2009WR008606.
[56] M. Torabi, N. Karimi, G.P. Peterson, S. Yee, Challenges and progress on the modelling of entropy generation in porous media: A review, International Journal of Heat and Mass Transfer. 114 (2017) 31–46. https://doi.org/10.1016/j.ijheatmasstransfer.2017.06.021.
[57] K. Vafai, ed., Porous media: applications in biological systems and biotechnology, CRC Press, Boca Raton, FL, 2011.
[58] P. Vadász, ed., Emerging topics in heat and mass transfer in porous media: from bioengineering and microelectronics to nanotechnology, Springer, Dordrecht, 2008.
[59] C.I. Voss, C.T. Simmons, N.I. Robinson, Three-dimensional benchmark for variable-density flow and transport simulation: matching semi-analytic stability modes for steady unstable convection in an inclined porous box, Hydrogeol J. 18 (2010) 5–23. https://doi.org/10.1007/s10040-009-0556-6.
[60] Q.W. Wang, J. Yang, M. Zeng, G. Wang, Three-dimensional numerical study of natural convection in an inclined porous cavity with time sinusoidal oscillating boundary conditions, International Journal of Heat and Fluid Flow. 31 (2010) 70–82. https://doi.org/10.1016/j.ijheatfluidflow.2009.11.005.
[61] A. Younes, P. Ackerer, F. Delay, Mixed finite elements for solving 2-D diffusion-type equations, Rev. Geophys. 48 (2010) RG1004. https://doi.org/10.1029/2008RG000277.
[62] A. Younes, M. Fahs, B. Belfort, Monotonicity of the cell-centred triangular MPFA

method for saturated and unsaturated flow in heterogeneous porous media, Journal of Hydrology. 504 (2013) 132–141. https://doi.org/10.1016/j.jhydrol.2013.09.041.
[63] C. Zhao, B. E. Hobbs, A. Ord, S. Peng, H. B. Mühlhaus, L. Liu, Double diffusion-driven convective instability of three-dimensional fluid-saturated geological fault zones heated from below, Mathematical Geology. 37 (2005), 373–391. https://doi.org/10.1007/s11004-005-5954-2.
[64] C. Zhao, B. E. Hobbs, A. Ord, Fundamentals of computational geoscience: numerical methods and algorithms, Springer, Berlin, 2009.
[65] Y.J. Zhuang, Q.Y. Zhu, Numerical study on combined buoyancy–Marangoni convection heat and mass transfer of power-law nanofluids in a cubic cavity filled with a heterogeneous porous medium, International Journal of Heat and Fluid Flow. 71 (2018) 39–54. https://doi.org/10.1016/j.ijheatfluidflow.2018.03.006.